Salt-concentrated acetate electrolytes for a high voltage aqueous Zn/MnO_2 battery

*Shigang Chen [a], Rong Lan [a,c] John Humphreys [a] and Shanwen Tao [a,b]**

[a] *School of Engineering, University of Warwick, Coventry CV4 7AL, UK*
[b] *Department of Chemical Engineering, Monash University, Clayton, Victoria 3800, Australia*
[c] *Faculty of Engineering, Environment & Computing, Coventry University, Coventry, CV1 5FB, UK*

Abstract

Aqueous rechargeable Zn/MnO_2 batteries are attractive due to their low-cost, high safety and use of non-toxic materials. In terms of electrolyte materials, it is anticpated that an aqueous electrolyte with a wider electrochemical window will improve the stablity and energy density. In this work, we investgated salt-concentrated electrolytes based on relatively inexpensive acetate salts. An electrochemical window of 3.4 V was achieved in salt-concentrated 1 m $Zn(OAc)_2$+31 m KOAc electrolyte. Its total ionic conductivity is 2.96×10^{-2} S·cm^{-1} while the ionic conductivity of Zn^{2+} ions is 7.80×10^{-3} S·cm^{-1}, estimated by a current interrupt method. This electrolyte is regarded as a mild alkaline enviroment with a pH value of 9.76, resulting in a different storage mechanism for anode with Zn stripping/deposition and cathode with proton intercalation/deintercalation. A Zn/MnO_2 battery was assembled using 1 m $Zn(OAc)_2$+31 m KOAc electrolyte, self-supported α-MnO_2-TiN/TiO_2 cathode and Zn foil anode. The Zn/MnO_2 battery can be charged to 2.0 V versus Zn/Zn^{2+} and delivers a discharge capacity and energy density of 304.6 $mAhg^{-1}$ (MnO_2) or 0.32 mAh·cm^{-2} (calculated on the area of electrode), and 368.5 (based on MnO_2) or 232.7 Wh·kg^{-1} (calculated on the total active mass of electrodes and electrolyte) in the first cycle under a current density of 100 mA·g^{-1} (~ C/3, based on MnO_2) or 0.1 mA·cm^{-2} (based on the area of electrode). During cycling, the coulombic efficiency can be maintained around 99% and reached 99.9 % during the 14-340th cycles. After the cycling tests, almost no dendrites were observed on the Zn foil anode attributing to the super-high salt concentration in that acetate-based electrolyte, which will benefit the stability of aqueous Zn/MnO_2 batteries.

Keywords: aqueous rechargeable battery, Zn/MnO_2, acetates, salt-concentrated electrolytes, WiBSE

---

* Corresponding author
E-mail: to be added

1. Introduction

Batteries are important electrochemical devices for energy storage [1, 2]. Of the various developed batteries, lithium ion batteries (LIBs) are the most popular due to their high energy density [3-6]. The electrolytes for conventional LIBs usually consist of $LiPF_6$, $LiCF_3SO_3$, or $LiBF_4$ salts and propylene carbonate, ethylene carbonate, polyethylene oxide and dimethyl carbonate organic solvents, which are expensive, flammable and not environmentally benign [6, 7]. Considering this associated challenge on both cost and safety, in 1994, the first aqueous lithium-ion battery using 5 M $LiNO_3$ aqueous solution as the electrolyte was developed [8], with great progress made in recent years [9, 10]. However, element lithium on the earth is a limited resource, which could create an issue for large scale applications of LIBs. The biggest advantage of LIBs is their high energy density, which is desired for transport applications. For stationary energy storage, such as grid-scale energy storage, the requirement on energy density is not as high with cost and safety being the key aspects[11]. Therefore researchers have extended their research to include batteries based on earth abundant elements such sodium (Na), potassium (K), zinc (Zn) etc. [1, 12-14]. Among these elements, Zn^{2+}-ion based batteries, particularly aqueous rechargeable batteries (ARBs) using Zn^{2+} ions as the charge carriers, have attracted great attention. This is due to their low-cost, high safety, low redox potential (-0.76 V vs. standard hydrogen electrode (SHE)), and potentially high energy density [5, 15, 16].

As for the electrode materials for aqueous rechargeable Zn^{2+}-ion batteries (ARZiBs), the negative electrode is normally Zn foil or Zn powders. The typical positive electrode materials for ARZiBs can be classified into manganese-based oxides, vanadium-based materials and Prussian blue analogues [17-19]. Among these positive electrode materials, manganese-based oxides such as MnO_2 have been shown to be good candidates for assembling ARZiBs with relatively high voltages (around 1.8 V for neutral or mild acidic electrolytes and around 1.6 V for alkaline electrolytes) [20, 21]. As the energy density of a battery is related to the cell voltage, these aqueous Zn/MnO_2 batteries have relatively high energy densities [5]. However, the charge/discharge mechanism and performance of MnO_2 is dependent on the particle size and the difference in crystallographic polymorphs (α, β, γ, δ, λ, and amorphous)[22]. In addition, aqueous rechargeable Zn/MnO_2 batteries usually exhibit poor stability and restricted energy density due to water splitting in the aqueous electrolytes providing further challenges [23, 24]. To handle these challenges, a core-shell structure was designed and applied into the MnO_2

cathode[25]. A quasi-solid state electrolyte was also employed by introducing poly(vinyl alcohol) (PVA) into the aqueous electrolyte to minimize the water content and enhance the cyclic stability of the Zn/MnO_2 battery[26]. In general, minimising the water splitting reaction during the charge/discharge of a battery can provide an excellent strategy to widen the electrochemical stability window of the aqueous electrolyte. Recently, a new type of salt-concentrated battery electrolyte moved to the forefront by simply increasing the salt concentration in suitable salt–solvent combinations, which can bring about an excellent rate capability, high energy density and stable operation to various electrochemical storage devices[27]. For ARBs, salt-concentrated electrolytes with 21 m (molality, mol-salt in kg-solvent) lithium bis(trifluoromethane sulfonyl)imide (LiTFSI) salt dissolved in water were also proposed as 'water-in-salt' electrolytes (WiSE) to widen its stability window to 3.0 V [28]. Meanwhile, hydrate-melt electrolytes which were reported by Yamada's group, which are optimized eutectic systems of LiTFSI and lithium bis(perfluoroethysulfonyl)imide (LiBETI), showed that a room-temperature hydrate melt of Li salts can be used as a stable aqueous electrolyte (and even can reach 3.8 V operation voltage) in which all water molecules participate in the Li^+ hydration shells while retaining fluidity [29].

Although wide electrochemical stability windows for aqueous electrolytes have been achieved on these expensive organic salts, the high cost could be a potential obstacle for large scale application of these electrolytes. Therefore, in terms of cost, aqueous electrolytes based on inexpensive salts would be a better choice. Aqueous solutions of salts such as $LiNiO_3$ and KOAc have been investigated as the potential electrolytes for ARBs [8, 30-32]. It has been reported that cost-effective concentrated potassium acetate (KOAc) aqueous solution (31 m) exhibits an electrochemical stability window of 3.2 V [31]. LiOAc was added into the concentrated KOAc solution to form 32 m KOAc+8 m lithium acetate (LiOAc) mixed cation acetate 'water-in-bisalt' electrolyte (WiBSE). This electrolyte has an electrochemical stability window of ~ 3.0 V providing a Li^+-ion based ARB [32]. Based on a similar strategy, in this study, we develop aqueous Zn^{2+}-ion conductors with wide electrochemical stability windows to be used as electrolytes for high voltage Zn/MnO_2 batteries. Both zinc acetate ($Zn(OAc)_2$) and KOAc were dissolved in water at room temperature to form a 1 m $Zn(OAc)_2$ + 31 m KOAc aqueous acetate solution. The as-formed salt-concentrated aqueous electrolyte also meets the definition of WiBSE [28]. The electrochemical stability window at room temperature of the mixed 1m $Zn(OAc)_2$ + 31 m KOAc electrolyte is around 3.4 V. This electrolyte is assembled

with a self-supported α-MnO_2-TiN/TiO_2 cathode (nanosized α-MnO_2 particles grown on the porous TiN/TiO_2 substrate directly via a hydrothermal reaction) and polished zinc foil as the anode, completing the Zn/MnO_2 battery. The Zn/MnO_2 battery was demonstrated as a hybrid battery, in which Zn^{2+} was stripped/deposited on the Zn foil anode with a slight reaction between Zn and OH^- and proton intercalated/deintercalated in the MnO_2 cathode. Through the electrochemical characterization, the Zn/MnO_2 battery delivered a discharge capacity of 304.6 $mAh \cdot g^{-1}$ (1.2 mg MnO_2) or 0.31 mAh cm^{-2} (1.13 cm^2 electrode area) and an energy density of 232.7 $Wh \cdot kg^{-1}$ (based on the total active mass of electrodes and electrolyte) on the first cycle, and a discharge capacity of 243.1 $mAh \cdot g^{-1}$ or 0.26 mAh cm^{-2} and an energy density of 175.5 $Wh \cdot kg^{-1}$ after 600 cycles, with capacity retention of 79.7% when charged/discharged at a current density 100 $mA \cdot g^{-1}$ (0.1 mA cm^{-2}). The cut-off voltage was 2 V which is higher than the normally reported values 1.8 V or 1.6 V [17, 20, 21, 26, 33]. Dendrite was not observed at the Zn foil anode after cyclic and rate performance, attributing to the superiority of salt-concentrated electrolytes. This is a promising type of high voltage aqueous Zn/MnO_2 battery, having the potential for stationary energy storage.

2. Experimental

2.1. Preparation of 1 m $Zn(OAc)_2$+31 m KOAc salt-concentrated electrolytes and self-supported α-MnO_2 - TiN/TiO_2 cathode

The electrolyte (1 m $Zn(OAc)_2$+31 m KOAc) was prepared by dissolving $Zn(OAc)_2 \cdot 2H_2O$ (Sigma Aldrich, ACS, 98.0-101.0%) and KOAc (Alfa Aesar, 99%) in deionized water at room temperature to get a transparent saturated aqueous solution. Before synthesizing the self-supported MnO_2-TiN/TiO_2 cathode, TiN/TiO_2 porous substrate was prepared with titanium powder (Alfa Aesar, -200 mesh, 99.5%), KCl (Alfa Aesar, 98%), polyethylene glycol (Alfa Aesar, PEG 1500), poly methyl methacrylate (Alfa Aesar, PMMA) and stearic acid (Alfa Aesar, Reagent Grade) by hot press at 150℃ firstly to obtain pellets followed by calcination under N_2 at 1200 ℃ for 2 hours [34]. In order to grow nanosized MnO_2 on porous TiN/TiO_2 substrate, 0.04 g sodium dodecyl sulfate (SDS, Sigma-Aldrich, ACS reagent) was dissolved in 10 mL deionized water, then 20 ml of 0.02 $g \cdot mL^{-1}$ $KMnO_4$ (Sigma-Aldrich, ACS reagent) solution was added dropwise and stirred for 15 min to gain a homogeneous solution. Subsequently, the mixed solution was transferred into a 40 mL polytetrafluoroethylene (PTFE) liner. The

TiN/TiO_2 porous substrate was transferred to the PTFE liner. The sealed autoclave was kept at 130℃ for 10 h. The autoclave was then cooled to the room temperature and the prepared electrode was washed by deionized water several times before drying in a vacuum oven at 50℃ for 24 h. Finally, the sample was annealed in 99.99% Ar (BOC) at 400℃ for 2 hours to achieve a better crystallized phase [35]. Finally, the active mass of MnO_2 was determined as 1.2 mg.

2.2. Assembly of Zn|1 m $Zn(OAc)_2$+31 m KOAc|MnO_2-TiN/TiO_2 full cell

Commercial zinc foil was polished by zinc powder (Alfa Aesar, median 6-9 micron, 97.5%) for approximately 10 min, then washed with soap and deionized water, rinsed with 2-proponal and dried at 60℃ in a vacuum oven for 3 h [36]. Both the Zn anode and MnO_2 on TiN/TiO_2 porous substrate were cut into round shape discs with 12 mm in diameter using a precision disc cutting machine (Kejing, MSK-T10), while the glass microfiber filter (Whatman) was cut into a 16 mm-diameter disc to be used as a separator. Finally, the anode, cathode and separator were assembled together in the CR2016 coin cell by the hydraulic crimping machine (Kejing, MSK-110) with 350 μL 1 m $Zn(OAc)_2$+31 m KOAc electrolyte.

2.3. Material Characterization

Thermo Scientific STAR A214 pH meter was employed to test pH values of different acetate-based aqueous solutions. Fourier-transform infrared spectroscopy (FTIR) measurements were carried out on a Bruker Vertex 70V IR spectrometer. The X-ray diffraction (XRD) patterns of zinc foil and TiN/TiO_2 porous substrate were collected on a PANanalyticalX'Pert Pro in the Bragg-Brentano reflection geometry with a Ni-filtered Cu Kα source (1.5405 Å), fitted with the X'Celerator detector and an Empyrean CuLFF xrd tube. In order to collect the XRD data of MnO_2 nanoparticles, Panalytical Empyrean equipped with a Co target was employed to avoid the fluorescence. For both XRD devices, absolute scans in the 2θ range of 10–90° with step sizes of 0.0167° were used during data collection. Small-angle X-ray scattering (SAXS) and wide-angle X-ray scattering (WAXS) were utilized for detecting the particle size and phase of nanosized MnO_2 before and after charge-discharge reaction with a 5m Xenocs Xeuss 2.0 SAXS instrument, equipped with Mo sources and a Pilatus 300K hybrid photon counting detector. Scanning electron microscopy (SEM) measurements were carried out on a ZEISS SUPRA 55-VP Field Emission Scanning Electron Microscope equipped with an energy dispersive X-ray (EDX) spectrometer for elemental composition analysis.

2.4. Electrochemical measurements

A Solartron 1470E multichannel cell test system was employed to test both cyclic voltammogram (CV) to determine the redox peaks of the anode and cathode. Linear sweep voltammetry (LSV) curves of the acetate-based electrolytes were measured to determine their electrochemical windows. For LSV tests, two commercial Ti foils were ultrasonically washed in 5 wt% hydrochloric acid and 2-propanol before insertion into the acetate-based electrolytes as the working and counter electrodes respectively, while Ag/AgCl (in saturated KCl) was used as the reference electrode. Electrochemical impedance spectroscopy (EIS) was employed to obtain the total conductivity of various electrolytes through an integrated Solartron 1455A frequency response analyzer with 10 mV bias and a frequency range of 100 kHz-0.1 Hz. The geometry factor of the cell for conductivity measurements was predetermined at 25℃ using 0.1 M aqueous KCl standard solution. To determine the real ionic conductivity of Zn^{2+} ion in the 1 m $Zn(OAc)_2$+31 m KOAc electrolyte owning various kinds of charge carriers, a current interrupt method was utilized with 1.0 V vs. Zn/Zn^{2+} applied voltage to a Zn/Zn symmetric cell based on that electrolyte. In comparison of the resistance of the acetate-based electrolyte and 0.1 M KCl standard solution with same dimensions, the ionic conductivity of Zn^{2+} ion can be estimated. After the CR2016 coin cells were assembled, they were relaxed under prescribed cut-off conditions for 8 h until they obtained a relative equilibrium condition. Galvanostatic cycling and rate capability measurements with potential limitation (2.0 – 0.8V versus Zn/Zn^{2+}) were carried out using an 8-channel Land CT2001A battery test system at room temperature. The capacity and energy density of the Zn/MnO_2 cells were calculated based on the mass of MnO_2 following the previous reports [26, 37, 38], finally, their energy density was obtained through integration of the discharge curve.

3. Results and discussion

3.1. Properties of mixed cation acetate salt-concentrated aqueous electrolytes

In order to investigate the relationship between the salt concentrations and electrochemical stability windows of the mixed cation acetate-based aqueous electrolytes, 1 m $Zn(OAc)_2$ (1.5 m of which already had some precipitation shown in Supporting Information, Fig. S1), 1 m $Zn(OAc)_2$+5 m KOAc, 1 m $Zn(OAc)_2$+10 m KOAc, 1 m $Zn(OAc)_2$+20 m KOAc and 1 m

$Zn(OAc)_2$+31 m KOAc were tested respectively via LSV at a scanning rate of 1 $mV \cdot s^{-1}$. The measured electrochemical stability windows are shown in Fig.1a. Clearly, the stability window becomes wider with increased salt concentration, from 2.6 V for 1 m $Zn(OAc)_2$ to 3.4 V for 1 m $Zn(OAc)_2$+31 m KOAc (Table S1). In the investigated samples, 1 m $Zn(OAc)_2$+31 m KOAc exhibits the widest stability window thus is selected as the electrolyte for an aqueous Zn/MnO_2 battery. The rate performance under various scanning rates from 1 to 20 $mV \cdot s^{-1}$ of 1 m $Zn(OAc)_2$+31 m KOAc electrolyte was measured through an LSV method (Supporting Information, Fig. S2). The onset of negative Zn plating does change at different scanning rates while the onset for negative oxygen evolution reaction (OER) decreases at higher scanning rates. This indicates that it is required to keep the scanning rate low in order to have a wide electrochemical stability window. The ionic conductivity of these electrolytes was measured by EIS, utilizing 0.1 m KCl aqueous solution (the conductivity of 0.1 m KCl aqueous solution is 1.28×10^{-2} $S \cdot cm^{-1}$ at room temperature[39]) with the same dimensions (20 mL) and same set-up as the calibration sample. The recorded a.c. impedance spectra are shown in the Supporting Information, Fig. S3a. The ionic conductivity is 1.53×10^{-2} $S \cdot cm^{-1}$ for 1 m $Zn(OAc)_2$, to 2.96×10^{-2} $S \cdot cm^{-1}$ for 1 m $Zn(OAc)_2$+31 m KOAc (Table S1). To get an accurate tendency of ionic conductivity with the raising of KOAc concentration, ionic conductivity of 1 m $Zn(OAc)_2$+3 m KOAc (8.68×10^{-2} $S \cdot cm^{-1}$), 1 m $Zn(OAc)_2$+7 m KOAc (1.11×10^{-1} $S \cdot cm^{-1}$), 1 m $Zn(OAc)_2$+15 m KOAc (7.57×10^{-2} $S \cdot cm^{-1}$) and 1 m $Zn(OAc)_2$+25 m KOAc (2.43×10^{-2} $S \cdot cm^{-1}$) were measured by EIS and added in Fig. S3a, while the relevant tendency is shown in Fig. S3b. With increased KOAc concentration, the ionic conductivity increases at first achieving a maximum at 1 m $Zn(OAc)_2$+7 m KOAc due to the raising of charge carriers in the electrolytes, then decreases due to the soaring of viscosity of electrolytes [40]. It is noteworthy that, the conductivity of 1 m $Zn(OAc)_2$+31 m KOAc electrolyte measured by EIS is the total conductivity which included the conductivity of all the charge carriers such as Zn^{2+}, K^+, OAc^-, H^+ and OH^- ions. Therefore, to confirm the ions interaction effect caused by ions other than the Zn^{2+} ion, the transference number of Zn^{2+} ($T_{Zn^{2+}}$) of various electrolytes was tested by the current interrupt method. This was carried out in a Zn/Zn symmetric cell with various electrolytes using Zn foils working as reversible electrodes for Zn^{2+} ions, while also serving as blocking electrodes for other ions. $T_{Zn^{2+}}$ can be determined by the initial current (I_o) and final steady-state current (I_s) of current interrupt method with the following equation[41]:

$$T_{Zn^{2+}} = \frac{Is}{Io} \quad (1)$$

As shown in Supporting Information, Fig. S3c, after applying 1.0 V vs. Zn/Zn^{2+}, the current of all the Zn/Zn symmetric cells with various electrolytes drops except for the cell with 1 m $Zn(OAc)_2$ electrolyte, the current of which remains around 0.025 A. In Fig. S3d, $T_{Zn^{2+}}$ decreased with the increased concentration of KOAc, from 1 for 1 m $Zn(OAc)_2$ to 0.38 for 1 m $Zn(OAc)_2$+31 m KOAc. The activity of Zn^{2+} ions in the electrolyte is suppressed in the presence of a high concentration of KOAc. From the current interrupt method, conductivity of Zn^{2+} ions can be estimated by comparing the resistance of Zn/Zn symmetric cells with 1 m $Zn(OAc)_2$+31 m KOAc electrolyte, keeping the same set-up and dimension of 0.1 m KCl standard solution. The ohmic resistance caused by Zn^{2+} ion migration can be calculated as 83.3 Ω, hence the ionic conductivity of Zn^{2+} ions can be estimated as 7.80×10^{-3} $S\cdot cm^{-1}$. The Zn^{2+} ionic conductivity is high enough to be used as an electrolyte for Zn^{2+} ion batteries. The ionic conductivity of Zn^{2+} ions in the salt-concentrated 1 m $Zn(OAc)_2$+31 m KOAc solution is lower than the total ionic conductivity of 1 m $Zn(OAc)_2$, which is 1.53×10^{-2} $S\cdot cm^{-1}$ (Table S1). Whereas, the conductivity of Zn^{2+} ions in 1 m $Zn(OAc)_2$ is estimated as 1.66×10^{-2} $S\cdot cm^{-1}$ by the current interrupt method, which is comparable to the value of 1.53×10^{-2} $S\cdot cm^{-1}$ obtained through EIS measurement. The activity of Zn^{2+} ions decreases in the presence of a high concentration of other ions such as K^+ and OAc^- ions, leading to reduced Zn^{2+} ionic conductivity.

On the LSV curves shown in Fig. 1a, the onsets (rapid accelerating) of the negative side (Zn plating) can be differentiated easily, whereas onsets at the positive sides (OER), especially for those of samples 1 m $Zn(OAc)_2$+5 m KOAc and 1 m $Zn(OAc)_2$+10 m KOAc, 1 m $Zn(OAc)_2$+20 m KOAc and 1 m $Zn(OAc)_2$+31 m KOAc, are very difficult to distinguish. Therefore, Tafel curves in high polarization areas were used to study OER kinetics of Ti foil electrodes in these four electrolytes. Based on the EIS plot in Supporting Information, Fig. S3a, the series resistance of those electrolytes can be determined as 6.27, 6.47, 11.86 and 21.26 Ω for samples 1 m $Zn(OAc)_2$+5 m KOAc and 1 m $Zn(OAc)_2$+10 m KOAc, 1 m $Zn(OAc)_2$+20 m KOAc and 1 m $Zn(OAc)_2$+31 m KOAc respectively. They are converted into the relevant *IR* to calculate their Tafel slopes. The Tafel curves derived from the corresponding LSV curves within the potential ranging from 1.95 to 2.0 V were converted into versus reversible hydrogen electrode (RHE) with *IR* eliminated are shown in Fig.1 b. The Tafel slopes of 1 m $Zn(OAc)_2$+5 m KOAc, 1 m $Zn(OAc)_2$+10 m KOAc, 1 m $Zn(OAc)_2$+20 m KOAc and 1 m $Zn(OAc)_2$+31 m

KOAc electrolytes are calculated as 114.9, 136.1, 141.1 and 147.6 $mV \cdot dec^{-1}$ respectively, indicating decreased OER kinetics from 1 m $Zn(OAc)_2$+5 m KOAc to 1 m $Zn(OAc)_2$+31 m KOAc (the larger the slope, the lower the activity[42]). The high concentration of acetates present supress the OER reaction thus extend the electrochemical stability window. The exchange current densities of all these electrolytes at theoretical potential for both OER (Fig. S4a) and HER (Fig. S4b) were investigated through the corresponding low polarization area of their Tafel curves to demonstrate their stability. The exchange current densities of 1 m $Zn(OAc)_2$, 1 m $Zn(OAc)_2$+5 m KOAc, 1 m $Zn(OAc)_2$+10 m KOAc, 1 m $Zn(OAc)_2$+20 m KOAc and 1 m $Zn(OAc)_2$+31 m KOAc at the OER side are 4.37×10^{-5}, 6.17×10^{-6}, 2.09×10^{-5}, 4.68×10^{-6} and 1.78×10^{-5} $A \cdot cm^{-2}$ respectively, while those at the HER side are 8.91×10^{-5}, 3.80×10^{-5}, 2.45×10^{-5}, 1.32×10^{-5} and 1.23×10^{-5} $A \cdot cm^{-2}$ respectively. The exchange current density of HER gradually decreases with increased KOAc concentration indicating the HER reaction is suppressed. However, the data for exchange current density of OER is not conclusive indicating the suppressing effect on the OER reaction is less significant, compared to that for HER.

According to previous reports, a local structure of intimate Li^+-water interaction will be enhanced at high salt concentrations in the Li^+-ion aqueous electrolytes, generating $(Li^+(H_2O)_2)n$ polymer-like chains, solidifying as the hydrates melt and induce wider stability windows[43]. Similar situations may happen on the salt-concentrated 1 m $Zn(OAc)_2$+31 m KOAc electrolyte. FTIR was used to characterize the liquid structure of these aqueous electrolytes in order to confirm the relationship between their structures and stability windows. The FTIR spectra of these aqueous electrolytes are exhibited in Fig.1c while those of the original chemicals are shown in Supporting Information, Fig. S5. The peaks observed from ca. 2900-3600 cm^{-1} in Fig.1 c represent the O-H stretching vibration bands involved in the hydrogen bonding[44], which gradually decrease when the concentration of salts in the aqueous electrolytes are increased. The peaks of ca. 1560, 1390 and 1330 cm^{-1} are assigned to asymmetric and symmetric stretching vibrations of the carboxylate group from the acetate anions. CH_3 asymmetric deformation[44] is increased and sharpened, coupling the increased concentration of the solution. Both changes indicate the phase out of hydrogen bonds and semi-solidification of salt-concentrated electrolytes[43].

Among the investigated salt-concentrated electrolytes, 1 m $Zn(OAc)_2$+31 m KOAc solution also meets the definition of WiBSE [31, 32] and is therefore a kind of WiBSE too. For ARBs,

the pH value of aqueous electrolytes can significantly affect their performance[45]. As for Zn/MnO_2 ARBs, depending on their pH value, there are two kinds of reaction mechanisms, Zn^{2+} (with H^+) ion insertion/desertion for neutral or mild acidic electrolytes and OH^- conversion for alkaline electrolytes[17, 20]. Therefore, the pH value of those aqueous electrolytes was measured by a Thermo Scientific STAR A214 pH meter (Fig. 1 d). The pH value of 1 m $Zn(OAc)_2$ is 5.71, which gradually increases with the increased concentration of alkaline KOAc solution, reaching 9.76 for the sample 1 m $Zn(OAc)_2$+31 m KOAc. This is a mild alkaline condition, which may induce OH^- as charge carriers in this electrolyte[46]. However, the real mechanism of Zn/MnO_2 ARBs, based on 1 m $Zn(OAc)_2$+31 m KOAc salt-concentrated electrolyte, can be determined by the CV and charge-discharge curves of both the MnO_2 cathode and Zn anode.

3.2. Redox mechanism and reversibility of Zn anode

To study the redox mechanism and reversibility of the Zn anode, a Zn/Ti coin cell (12 mm in diameter) was prepared based on the various electrolytes to discover the influence KOAc concentration has on the CE of Zn stripping/plating. CV tests were carried out within the potential range of -0.6 to 0.6 V versus Zn/Zn^{2+}, at a scanning rate of 1 $mV \cdot s^{-1}$. The CV curves and relevant chronocoulometry curves of Zn/Ti coin cell with 1 m $Zn(OAc)_2$+31 m KOA electrolyte are shown in Fig. 2a and b, respectively. In the first CV cycle, the redox peaks are at 0.26 and -0.22 V versus Zn/Zn^{2+} coupling with 82.1% coulombic efficiency (CE) derived from chronocoulometry curves, while the peaks shifted to 0.2 and -0.2 V versus Zn/Zn^{2+} in the second CV cycle and stayed at that position in the following cycles. This indicates that the Zn stripping/plating reaction is achieved in this electrolyte, which is a mild alkaline environment[47]. Meanwhile, the CEs increase from 91.2% in the second CV cycle to 99.0% in the 5^{th} CV cycle, which demonstrates the feasibility and reversibility of Zn stripping/plating (Fig. 2b). The CV curves and relevant chronocoulometry curves of Zn/Ti coin cells with other electrolytes are shown in Fig. S6. In general, the CEs increases with the increased concentration of KOAc. To confirm the reversibility and stability of Zn in the 1 m $Zn(OAc)_2$+31 m KOAc electrolyte, Zn/Zn symmetric cell was made and tested for 200 cycles (ca. 2000 min) under galvanostatic condition with a current density of 5 $mA \cdot cm^{-2}$. Before the test, the polished Zn foil is characterized via SEM with a smooth surface exhibited as shown in Supporting Information, Fig. S7. In Fig. 2c, the charge-discharge curves are displayed with potential limitation of -0.2 to 0.2 V versus Zn/Zn^{2+} according to the position of redox peaks on CV

curves[47], and CE of every cycle is shown in its inset figure, in which the CE of the first cycle is 64.2% increasing to 99.1% in the 19th cycle. The CEs maintains around 99.0% in the following cycles until the 200th cycle (99.2% CE). This delivers the desired reversibility and stability. The average capacity for the Zn stripping/plating is about 0.8 mAh·cm^{-2} which is enough to assemble a full cell with our α-MnO_2-TiN/TiO_2 cathode (no more than 0.5 mAh·cm^{-2} capacity), while that Zn stripping/plating capacity is still considerable according to previous reports [47, 48]. The tested Zn foil was characterized by SEM, EDX and XRD with the results shown in Supporting Information, Fig. S8. After the test, no dendrites on the Zn foil were found (Fig. S8a). The EDX element analysis (Fig. S8b), mapping (Fig. S8c) and XRD patterns of Zn foil of Zn/Zn symmetric cell after the cycling test (Fig. S8d), jointly confirm the major phase is Zn (ICDD: 04-003-5561) despite the presence of a small amount of ZnO due to the slight reaction between Zn foil and limited amount of OH^- ions (~6×10^{-5} mol·L^{-1} calculated with the pH value of 9.76). Normally, the electrolyte of alkaline Zn/MnO_2 batteries induce considerable ZnO on Zn foil in a strong alkaline environment with OH^- concentration higher than 1 mol·L^{-1} [46, 49-51]. The concentration of OH^- ions in our electrolyte is four orders of magnitudes lower thus the reactivity will be reduced. These results demonstrate that the major reaction between Zn foil and 1 m $Zn(OAc)_2$+31 m KOAc salt-concentrated electrolyte is reversible Zn stripping/plating as shown in the following equation:

$$Zn \rightarrow Zn^{2+} + 2e^- \quad (2)$$

In order to further investigate the reaction mechanism, 31 m KOAc was prepared with the pH value of 11.05 then adjusted with acetic acid back to a pH value of 9.56, similar to that of 1 m $Zn(OAc)_2$+31 m KOAc. Zn/Zn symmetric cell was assembled with the pH value-adjusted 31 m KOAc electrolyte. The CV curves, galvanostatic Zn stripping/plating and XRD pattern of Zn in this cell are shown in Fig. S9. No considerable reaction between Zn and 31 m KOAc electrolyte with the adjusted pH value can be observed, and the reaction occurs when $Zn(OAc)_2$, especially Zn^{2+} ions are introduced, compared with the CV curves and galvanostatic Zn stripping/plating test on Zn/Zn symmetric cell using a 1 m $Zn(OAc)_2$+31 m KOA electrolyte in Fig.2. XRD was employed on the Zn foil of that Zn/Zn symmetric cell for post-mortem analysis with the result shown in Fig. S9d, demonstrating single phase of Zn (ICDD: 01-078-9363). The absence of ZnO in the XRD result indicates that the reaction between Zn and OH^- ions in the 31 m KOAc electrolyte is negligible, while the difference regarding the existence of ZnO between Fig. S8 and Fig. S9 is caused by the various time length of galvanostatic

charge-discharge test. The capacity limit of 2 $mAh \cdot cm^{-2}$ is set by us for the cycling test on the Zn symmetric cell under various current densities from 0.5 (5 cycles with 2 activation cycles), 1 (5 cycles), 2 (5 cycles) to 5 (10 cycles) $mA \cdot cm^{-2}$ respectively with 94 h test time in total to further demonstrate its stability and mechanism (Fig. 2d). After the symmetrical cell measurements, the tested Zn foils were characterized by SEM and XRD (Fig. 2d). No obvious dendrite was observed on Zn foil while the small (202) peak of ZnO (ICDD: 01-075-1526) can be found, attributing to the possible slight reaction between Zn foils and OH^-, while the main reaction between the Zn foil and electrolyte should still be Zn stripping/depositing due to the limited amount of OH^- ions in this salt-concentrated electrolyte.

3.3. Characterization on self-supported α-MnO_2-TiN/TiO_2 cathode

In our study, we choose MnO_2 as the positive electrode as it has a high capacity and can build a battery with relatively higher voltage. MnO_2 was directly grown on a home-made TiN/TiO_2 porous substrate which has been utilized in lithium-sulphur batteries with excellent redox stability [52]. The morphology of the as-prepared TiN/TiO_2 substrate is shown in the Supporting Information, Fig. S10a. It is composed of TiO_2 phase (ICDD: 03-065-1119) and TiN phase (ICDD: 04-069-8169) (Fig. S10b). XRD analysis on the deposited powders after hydrothermal reaction indicates α-MnO_2 (ICDD: 04-005-4884) was successfully grown on the TiN/TiO_2 porous substrate (Supporting Information, Fig. S11). SAXS was also utilized to analyse the particle size of α-MnO_2 powders in Supporting Information, Fig. S12 with lognormal distribution, showing a 24 nm mean size and 18 Å full width at half maximum (FWHM). The morphology and elements of MnO_2-TiN/TiO_2 cathode are characterized by SEM/EDX (Fig. 3). In Fig. 3a, the image with 50 μm resolution displays the morphology of nanosized MnO_2 particles on porous substrate whilst peaks for Ti, O, N, Mn and Si (caused by the conductive polymer film used to stick samples to the sample stage of SEM device), as exhibited in the inset EDX analysis. The particle size of nano-MnO_2 is less than 100 nm (Fig. 3b). The corresponding element mappings are shown in Fig 3c-f for elements Mn, O, N and Ti, respectively. Element Mn is distributed in the same location as the nanoparticles while elements N and Ti are evenly distributed on the whole substrate.

3.4. Performance of Zn/MnO_2 battery

Based on the results above, two half cells and a full Zn/MnO_2 coin cell based on 1 m $Zn(OAc)_2$+31 m KOAc electrolyte were fabricated, the properties of each electrode plus the whole cell were investigated as well. The CV curves of both the Zn anode and MnO_2-TiN/TiO_2 cathode were collected respectively (Supporting Information, Fig. S13), these were recorded at a scanning rate of 1 $mV \cdot s^{-1}$ within 5 cycles in a three-electrode cell separately. 1 m $Zn(OAc)_2$+31 m KOAc was used as the electrolyte, Ti foil as counter electrode, and Ag/AgCl as reference electrode. In Fig. 4a, the 5^{th} cycle of CV curves, both Zn anode and MnO_2-TiN/TiO_2 cathode, exhibit a pair of redox peaks happening at ~-0.95 and ~-1.1 V vs. Ag/AgCl (~0.03 and ~-0.12 V vs. Zn/Zn^{2+}), representing for the Zn plating/striping[53]. Meanwhile, the other pair of redox peaks at ~0.6 and ~0.3 V vs. Ag/AgCl (~1.58 and ~1.28 vs. Zn/Zn^{2+}) is due to the reversible conversion between MnO_2 and MnOOH caused by the proton intercalation/deintercalation in the alkaline environment [21, 33], which is proven by its charge-discharge curves and material characterization on the cathode after electrochemical measurements. To investigate the reaction mechanism of the cathode in 1 m $Zn(OAc)_2$+31 m KOAc electrolyte further, MnO_2-TiN/TiO_2, Ti foil and Ag/AgCl were utilized as working, counter and reference electrodes respectively. 31 m KOAc electrolyte adjusted by acetic acid to have similar pH value with that of the 1 m $Zn(OAc)_2$+31 m KOAc electrolyte, was utilized as electrolyte in the three-electrode system. As shown in Fig. S14, the redox couple around 0.6/0.3 V vs. Ag/AgCl, which coincides with the redox couple of MnO_2-TiN/TiO_2 cathode in the 1 m $Zn(OAc)_2$+31 m KOAc electrolyte (Fig.4a). The presence or absence of Zn^{2+} ions has little effects on the redox reaction at the MnO_2-TiN/TiO_2 cathode, indicating that Zn^{2+} ions may not participate in the reaction of MnO_2-TiN/TiO_2 cathode in our salt-concentrated electrolyte. Therefore, both Zn^{2+} and OH^- ions serve as charge carriers with hybrid mechanism for Zn-MnO_2 batteries based on the mild alkaline salt-concentrated electrolyte. Unlike the traditional 'rocking-chair' cathode for LiBs which works on the basis of the immigration of Li^+ ions between cathode and anode, this Zn/MnO_2 battery can be regarded as a hybrid ion battery as it involves the immigration of more than one type of ions between the electrolyte and electrodes with the total concentration of hybrid ions fixed to ensure the charge neutrality of the electrolytes[54]. Zn^{2+} ions take part in the Zn plating/stripping reaction on the anode side while H_2O in the aqueous electrolyte is the proton source for the intercalate/deintercalate in MnO_2 with the generation or depletion of OH^- ions on cathode side. In our Zn/MnO_2 battery, the charge carriers are Zn^{2+} ions between the anode and electrolyte, and OH^- ions combined with H_2O between the electrolyte and the cathode.

For the full cell test, the assembled Zn/MnO_2 coin cell was activated under 20 mA·g^{-1} current density within 20 charge-discharge cycles, as shown in Supporting Information, Fig. S15. The cyclic charge-discharge test was carried out under galvanostatic conditions in the potential range between 2.0 and 0.8 V vs Zn/Zn^{2+}. The initial specific charge/discharge capacity during activation was 299.1/480.1 mAh·g^{-1} (on the basis of 1.2 mg MnO_2 mass) with 62.3% CE. The capacity maintained around 315/308 mAh·g^{-1} with about 98.5% CE after the 15^{th} cycle. The capacity is slightly higher than the theoretical capacity of 308 mAh g^{-1} for MnO_2, based on the molecular weight of MnO_2 and one electron transfer [20]. This extra storage capacity could be related to the nano-sized α-MnO_2 cathode prepared in this study. This kind of interfacial ion storage mechanism has been observed in LIBs [55, 56]. However, it cannot be ruled out that a tiny amount of Zn^{2+} may also react with MnO_2 to realise two electron transfer leading to higher capacity.

The activated coin cell is further characterized by a cyclic charge-discharge test for 600 cycles under galvanostatic conditions with 100 mA·g^{-1} (1/3 C, on the basis of 1.2 mg MnO_2) current density (Fig. 4b). Its specific charge/discharge capacity in the first cycle is 309.4/304.6 mAh·g^{-1} with 99.0 % CE which is further improved to 99.9% after the 14^{th} cycle and maintained until the 340^{th} cycle, after which it slowly decreased to ~ 98% for the last 260 cycles. The specific charge/discharge capacity of the 600^{th} cycle is 247.5/243.1 mAh·g^{-1} with 98.2% CE, which displays 79.7% capacity retention, compared to the capacity of the first cycle. The slightly decreased CE after the 340^{th} cycle could be related to side reactions which need further investigation. In order to shorten the gap between our Zn/MnO_2 battery and battery industry, the specific capacity is converted into areal capacity on the basis of TiN/TiO_2 porous substrate and Zn foil with 12 mm diameter, thus, the areal capacity of first cycle and last cycle can be determined as 0.31 and 0.26 mAh cm^{-2}, respectively. The relevant charge-discharge curves of the cyclic test are shown in Fig. 4c. The corresponding capacity is consistent with the values shown in Fig. 4b. The charge/discharge flat plateau are ~1.4-~1.7 and ~1.2-~1.55 V vs. Zn/Zn^{2+} respectively, which are consistent with the redox couple of CV curve on the MnO_2-TiN/TiO_2 cathode shown in Fig. 4a. This is believed to be due to the proton intercalation/deintercalation in the MnO_2 electrode [33, 57]. The corresponding energy density is calculated via integrating the discharge curves in Fig. 4c, which is 368.5, 364.0, 360.6, 351.9, 321.4, 301.9 and 277.8 Wh·kg^{-1} (based on MnO_2) for first, 5^{th}, 10^{th}, 20^{th}, 100^{th}, 200^{th}, 400^{th} and 600^{th} charge-discharge cycles respectively. In this work, the cell voltage was further extended to 2.0 V, taking

advantage of the wide electrochemical stability window of the salt-concentrated 1 m $Zn(OAc)_2$+31 m KOAc used as the electrolyte. The energy density of that cell was therefore improved to 368.5 $Wh \cdot kg^{-1}$ in the first cycle, which is comparable to some recently published papers about Zn/MnO_2 batteries in mild acid and neutral environments based on MnO_2 cathodes, [11, 20, 58, 59] however, it is lower than the aqueous Zn-MnO_2 battery based on an acidic sulfate electrolyte [60]. In reported works, the typical discharge/charge voltage range is 1.8 V – 1.0 V for aqueous Zn-MnO_2 batteries except for recent work based on an acidic sulfate electrolyte [11, 20, 59, 60] . Taking advantage of the wide electrochemical stability window of the salt-concentrated electrolyte, our Zn-MnO_2 battery still exhibits good stability at a discharge-charge voltage of 2.0 V to 0.8 V. Compared to the reported aqueous Zn-MnO_2 batteries, this is a kind of over-charge and over-discharge. From this point of view, aqueous Zn-MnO_2 batteries based on salt-concentrated electrolytes are more robust.

The rate performance of the Zn-MnO_2 coin cell was tested under current densities of 100, 200, 400, 800, 1600 $mA \cdot g^{-1}$ (based on MnO_2) respectively. Accordingly, the specific charge/discharge capacity of the last cycle for each current density was determined as 240.1/237.6, 220.2/216.9, 190.5/187.5, 159.8/156.8 and 120.6/117.3 $mAh \cdot g^{-1}$ (based on MnO_2) respectively (Fig. 4d). It has been reported that, at mild acidic conditions, the stability of Zn-MnO_2 batteries at low C-rate is poor because of the irreversible conversion reaction at ~ 1.26 V, whilst the battery is much more stable at high C-rate [11]. In our Zn-MnO_2 coin cell, the electrolyte is a weak alkaline, the cycling stability of the battery at a current density of 100 $mA \cdot g^{-1}$ (~ C/3) is still quite good (Figure 4b). This may be related to the different reaction mechanisms in different reaction environments, which are discussed below.

The EIS spectra of the coin cell before and after cyclic and rate performance tests are compared in Supporting Information, Fig. S16. The series resistance of the electrolyte and interfacial resistance between electrolyte and electrode slightly increased after the measurements. After the electrochemical tests, both the cathode and anode are taken apart for post-mortem analyses. The FTIR spectra of the MnO_2-TiN/TiO_2 cathodes before and after the cycling are shown in Supporting Information, Fig. S17. The additional peaks at 490, 645 and 1620 cm^{-1} on the spectrum for the cathode after-cycling tests are attributed to the bands of the Mn-O vibrations and OH bending mode, indicating the possible presence of MnOOH [61]. Meanwhile, WAXS was employed to detect the phase transformation of that cathode before and after charge-discharge reaction (Supporting Information, Fig. S18). The groutite α-MnOOH (ICDD: 04-

010-4787)[62] was detected although the signal was quite weak. This indicates that, in our aqueous Zn/MnO_2 battery, the cathode reaction on discharge is [21],

$$MnO_2 + H_2O + e^- \rightarrow MnOOH + OH^- \quad (3)$$

However, in the real process, it is intercalation of protons into the MnO_2 to form MnOOH, even when a strong alkaline solution such as mixed KOH-LiOH was used as the electrolyte [33]. The source of proton is from neutral H_2O instead of H^+ ions. Negatively charged OH^- ions are formed through the intercalation of proton into MnO_2, therefore, OH^- ions are the charge carriers at the cathode. To further reveal this, the pH variation data of electrolyte during charge/discharge has been obtained in three-electrode cell with MnO_2-TiN/TiO_2 work electrode, Zn foil counter electrode and Ag/AgCl reference electrode as listed in Supporting Information, Fig. S19. It is observed that the pH value of that electrolyte is increased after the discharge reaction and decreased after the charge reaction except the first cycle charge-discharge reaction as there is no MnOOH to be oxidized into MnO_2 at the beginning, thus the charge capacity (93.1 $mAh \cdot g^{-2}$) is much lower than discharge capacity (415.3 $mAh \cdot g^{-2}$). The tendency of the pH value is consistent with proton insertion mechanism in MnO_2. The optical image of the pH meter is shown in Supporting Information, Fig. S19c. Due to the small quality (~350 μL) of the electrolyte used in the CR2016 coin cell, it is not enough to be directly measured by the pH meter therefore a three-electrode cell with 5 mL of electrolyte was utilized to demonstrate the trend of the pH value.

According to previous reports, under acidic or medium environment, Zn^{2+} ions (or combined with H^+ ions) will take part in the reaction at the cathode. The corresponding cathode reaction on discharge is[59]:

$$2MnO_2 + Zn^{2+} + 2e^- \rightarrow ZnMn_2O_4 \quad (4)$$

Under this reaction mechanism, it is expected that $ZnMn_2O_4$ will be generated at the cathode. However, in our research, $ZnMn_2O_4$ was not observed. From the results of FTIR and WAXS, the reaction at the cathode involves proton intercalation which yields MnOOH instead. This is consistent with the reaction mechanism shown in equation (2).

In the work of Liu's group, the mass of cathode, anode and electrolyte inclued in the electrochemical reaction was counted together for caculating the energy density, which is more relevant to industry[63]. Therefore, the energy density is re-calculated with the mass of active water and active zinc, after confirming reaction mechanism of our Zn/MnO_2 battery as equations (1) and (2). The mass of active water and active zinc are estimated under the circumstance of complete reaction through the following equation:

$$m_{active\ water} = m_{MnO_2} \times M_{H_2O}/M_{MnO_2} \approx 0.25\ mg \quad (5)$$

$$m_{active\ zinc} = m_{MnO_2} \times \frac{\frac{M_{Zn}}{M_{MnO_2}}}{2} \approx 0.45\ mg \quad (6)$$

Hence, 0.25 mg active water and 0.45 mg active zinc is involved for calculating energy density of our Zn/MnO_2 battery. Finally, the energy density of first and last cycles is re-calculated as 232.7 and 175.5 $Wh \cdot kg^{-1}$, which is impressive among the recent works about Zn/MnO_2 batteries using various calculation methods (as shown in the Supporting Information, Table S2)[26, 33, 60, 63-69]. Technically, there is still a gap between our Zn foil/nanosized MnO_2-TiN/TiO_2 battery and industrial application due to the low mass loading of MnO_2, which will be the task in our future work.

After the cycling test, the cathode was observed by SEM/EDS (Supporting Information, Fig. S20). The slight growth of the MnO_2 particles was observed after cycling, which may lead to the slow fade in capacity during the cycling. XRD spectra of Zn foil anodes before and after cycling are compared (Fig, 5a). No obvious difference in morphology was observed. For Zn foil anodes before and after the test, it is composed of Zn (ICDD: 01-078-9363) with a couple of weak peaks of ZnO (ICDD: 04-020-0364) due to the long-time slow reaction between Zn and OH^-. The SEM image of the cross section of the Zn anode after cycling is shown in Fig. 5b. The SEM image and corresponding layer mapping of Zn and O elements are shown in Figs. 5c and 5d respectively. Dendrite was not observed on the Zn anode after the cyclic test. For rechargeable batteries with metal anodes, dendrites induced by the uneven metal deposition can lead to thermal runaway and explosion hazards, which may limit their applications. The use of salt-concentrated 1 m $Zn(OAc)_2$+31 m KOAc electrolyte in our Zn/MnO_2 battery enhances the threshold of critical current density for cation depletion in the electrolyte thus suppressing the formation of zinc dendrites [70]. This is a key advantage of zinc batteries using salt-concentrated electrolytes, which may improve the stability and safety of aqueous batteries.

4. Conclusions

In this study, a new salt-concentrated 1 m $Zn(OAc)_2$+31 m KOAc electrolyte has been developed. It has an electrochemical stability window of 3.4 V. At room temperature, the mixed ionic conductivity of 1 m $Zn(OAc)_2$+31 m KOAc aqueous solution is 2.96×10^{-2} $S\cdot cm^{-1}$, while the ionic conductivity of Zn^{2+} ion measured by current interrupt method is 7.80×10^{-3} $S\cdot cm^{-1}$, which is high enough to be used as the electrolyte for batteries. Compared with other expensive organic salts, the acetate based salt-concentrated electrolyte has low cost and reduced toxicity. LSV, Tafel curves, EIS, FTIR and pH value tests were employed to investigate the properties of salt-concentrated 1 m $Zn(OAc)_2$+31 m KOAc electrolyte. A CR2016 coin cell using 1 m $Zn(OAc)_2$+31 m KOAc electrolyte, Zn foil anode and MnO_2-TiN/TiO_2 cathode was assembled. The battery can be charged to 2.0 V, taking advantage of the wide electrochemical stability window of the salt-concentrated 1 m $Zn(OAc)_2$+31 m KOAc electrolyte. The reaction and storage mechanisms of both anode and cathode were investigated in detail. The reaction mechanism of the investigated Zn/MnO_2 battery is a hybrid one with both Zn stripping/plating and proton intercalation/deintercalation involved due to the mild alkaline environment of this electrolyte. On the anode side, Zn^{2+} experiences Zn plating/stripping with slow reaction between Zn and OH^-, while proton intercalation/deintercalation in MnO_2 is used to achieve the reversible conversion between MnO_2 and MnOOH on the cathode side. The Zn/MnO_2 battery is characterized by cyclic and rate performance tests, which delivers desired stability, energy density and rate capability. Dendrite-free Zn foil anode is confirmed after cycling, attributing to the improved threshold critical current density for cations depleting in the new acetate-based salt-concentrated electrolyte.

Acknowledgements

To be added.

Appendix A. Supplementary material

Supplementary data associated with this article can be found in the online version at doi:10.1016/j.ensm.2019.xx.xxx.

References

[1] P. Tan, B. Chen, H.R. Xu, H.C. Zhang, W.Z. Cai, M. Ni, M.L. Liu, Z.P. Shao, Flexible Zn- and Li-air batteries: recent advances, challenges, and future perspectives, Energy Environ. Sci. 10 (2017) 2056-2080.

[2] P.G. Bruce, S.A. Freunberger, L.J. Hardwick, J.-M. Tarascon, Li-O_2 and Li-S batteries with high energy storage, Nature Materials 11 (2012) 19-29.

[3] M. Armand, J.-M. Tarascon, Building better batteries, Nature 451 (2008) 652-657.

[4] W.J. Yao, A.R. Armstrong, X.L. Zhou, M.T. Sougrati, P. Kidkhunthod, S. Tunmee, C.H. Sun, S. Sattayaporn, P. Lightfoot, B.F. Ji, C.L. Jiang, N.Z. Wu, Y.B. Tang, H.M. Cheng, An oxalate cathode for lithium ion batteries with combined cationic and polyanionic redox, Nature Communications 10 (2019) 3483.

[5] Z. Lin, T. Liu, X. Ai, C. Liang, Aligning academia and industry for unified battery performance metrics, Nature Communications 9 (2018) 5262.

[6] M. Li, J. Lu, Z. Chen, K. Amine, 30 years of lithium-ion batteries, Advanced Materials 30 (2018) 1800561.

[7] A. Manthiram, X. Yu, S. Wang, Lithium battery chemistries enabled by solid-state electrolytes, Nature Reviews Materials 2 (2017) 16103.

[8] W. Li, J.R. Dahn, D.S. Wainwright, Rechargeable Lithium Batteries with Aqueous Electrolytes, Science 264 (1994) 1115-1118.

[9] N. Alias, A.A. Mohamad, Advances of aqueous rechargeable lithium-ion battery: A review, Journal of Power Sources 274 (2015) 237-251.

[10] C. Yang, J. Chen, X. Ji, T.P. Pollard, X. Lü, C.-J. Sun, S. Hou, Q. Liu, C. Liu, T. Qing, Y. Wang, O. Borodin, Y. Ren, K. Xu, C. Wang, Aqueous Li-ion battery enabled by halogen conversion–intercalation chemistry in graphite, Nature 569 (2019) 245-250.

[11] Y. Li, S. Wang, J.R. Salvador, J. Wu, B. Liu, W. Yang, J. Yang, W. Zhang, J. Liu, J. Yang, Reaction mechanisms for long-life rechargeable Zn/MnO_2 batteries, Chemistry of Materials 31 (2019) 2036-2047.

[12] H. Kim, J. Hong, K.-Y. Park, H. Kim, S.-W. Kim, K. Kang, Aqueous rechargeable Li and Na ion batteries, Chemical Reviews 114 (2014) 11788-11827.

[13] C.D. Wessells, S.V. Peddada, R.A. Huggins, Y. Cui, Nickel hexacyanoferrate nanoparticle electrodes for aqueous sodium and potassium ion batteries, Nano Letters 11 (2011) 5421-5425.

[14] M. Yan, P. He, Y. Chen, S. Wang, Q. Wei, K. Zhao, X. Xu, Q. An, Y. Shuang, Y. Shao, K.T. Mueller, L. Mai, J. Liu, J. Yang, Water-lubricated intercalation in $V_2O_5{\cdot}nH_2O$ for high-capacity and high-rate aqueous rechargeable zinc batteries, Advanced Materials 30 (2018) 1703725.

[15] F. Ming, H. Liang, Y. Lei, S. Kandambeth, M. Eddaoudi, H.N. Alshareef, Layered $Mg_xV_2O_5{\cdot}nH_2O$ as cathode material for high-performance aqueous zinc ion batteries, ACS Energy Letters 3 (2018) 2602-2609.

[16] D. Kundu, B.D. Adams, V. Duffort, S.H. Vajargah, L.F. Nazar, A high-capacity and long-life aqueous rechargeable zinc battery using a metal oxide intercalation cathode, Nature Energy 1 (2016) 16119.

[17] C. Xu, B. Li, H. Du, F. Kang, Energetic Zinc Ion Chemistry: The Rechargeable Zinc Ion Battery, Angewandte Chemie Internatinal Edition 51 (2012) 933-935.

[18] G. Fang, J. Zhou, A. Pan, S. Liang, Recent advances in aqueous zinc-ion batteries, ACS Energy Letters 3 (2018) 2480-2501.

[19] Z. Liu, G. Pulletikurthi, F. Endres, A prussian blue/zinc secondary battery with a bio-ionic liquid–water mixture as electrolyte, ACS Applied Materials & Interfaces 8 (2016) 12158-12164.

[20] W. Sun, F. Wang, S. Hou, C. Yang, X. Fan, Z. Ma, T. Gao, F. Han, R. Hu, M. Zhu, C. Wang, Zn/MnO_2 battery chemistry with H^+ and Zn^{2+} coinsertion, Journal of the American Chemical Society 139 (2017) 9775-9778.
[21] F.Y. Cheng, J. Chen, X.L. Gou, P.W. Shen, High-power alkaline Zn–MnO_2 batteries using γ-MnO_2 nanowires/nanotubes and electrolytic zinc powder, Advanced Materials 17 (2005) 2753-2756.
[22] B. Lee, C.S. Yoon, H.R. Lee, K.Y. Chung, B.W. Cho, S.H. Oh, Electrochemically-induced reversible transition from the tunneled to layered polymorphs of manganese dioxide, Scientific Reports 4 (2014) 6066.
[23] C. Liu, X. Wang, W. Deng, C. Li, J. Chen, M. Xue, R. Li, F. Pan, Engineering Fast Ion Conduction and Selective Cation Channels for a High-Rate and High-Voltage Hybrid Aqueous Battery, Angewandte Chemie Internatinal Edition 57 (2018) 7046-7050.
[24] M.H. Alfaruqi, J. Gim, S. Kim, J. Song, J. Jo, S. Kim, V. Mathew, J. Kim, Enhanced reversible divalent zinc storage in a structurally stable α-MnO_2 nanorod electrode, Journal of Power Sources 288 (2015) 320-327.
[25] B. Wu, G. Zhang, M. Yan, T. Xiong, P. He, L. He, X. Xu, L. Mai, Graphene scroll-coated α-MnO_2 nanowires as high-performance cathode materials for aqueous Zn-ion battery, Small 14 (2018) 1703850.
[26] Y. Zeng, X. Zhang, Y. Meng, M. Yu, J. Yi, Y. Wu, X. Lu, Y. Tong, Achieving ultrahigh energy density and long durability in a flexible rechargeable quasi-solid-state Zn–MnO_2 battery, Advanced Materials 29 (2017) 1700274.
[27] Y. Yamada, J. Wang, S. Ko, E. Watanabe, A. Yamada, Advances and issues in developing salt-concentrated battery electrolytes, Nature Energy 4 (2019) 269-280.
[28] L. Suo, O. Borodin, T. Gao, M. Olguin, J. Ho, X. Fan, C. Luo, C. Wang, K. Xu, "Water-in-salt" electrolyte enables high-voltage aqueous lithium-ion chemistries, Science 350 (2015) 938-943.
[29] Y. Yamada, K. Usui, K. Sodeyama, S. Ko, Y. Tateyama, A. Yamada, Hydrate-melt electrolytes for high-energy-density aqueous batteries, Nature Energy 1 (2016) 16129.
[30] J.X. Zheng, G.Y. Tan, P. Shan, T.C. Liu, J.T. Hu, Y.C. Feng, L.Y. Yang, M.J. Zhang, Z.H. Chen, Y. Lin, J. Lu, J.C. Neuefeind, Y. Ren, K. Amine, L.W. Wang, K. Xu, F. Pan, Understanding Thermodynamic and Kinetic Contributions in Expanding the Stability Window of Aqueous Electrolytes, Chem 4 (2018) 2872-2882.
[31] D.P. Leonard, Z. Wei, G. Chen, F. Du, X. Ji, Water-in-salt electrolyte for potassium-ion batteries, ACS Energy Letters 3 (2018) 373-374.
[32] M.R. Lukatskaya, J.I. Feldblyum, D.G. Mackanic, F. Lissel, D.L. Michels, Y. Cui, Z. Bao, Concentrated mixed cation acetate "water-in-salt" solutions as green and low-cost high voltage electrolytes for aqueous batteries, Energy Environ. Sci. 11 (2018) 2876-2883.
[33] B.J. Hertzberg, A. Huang, A. Hsieh, M. Chamoun, G. Davies, J.K. Seo, Z. Zhong, M. Croft, C. Erdonmez, Y.S. Meng, D. Steingart, Effect of multiple cation electrolyte mixtures on rechargeable Zn–MnO_2 alkaline battery, Chemistry of Materials 28 (2016) 4536-4545.
[34] M.M. Shbeh, R. Goodall, Open pore titanium foams via metal injection molding of metal powder with a space holder, Metal Powder Report 71 (2016) 450-455.
[35] D. Yan, Z. Guo, G. Zhu, Z. Yu, H. Xu, A. Yu, MnO_2 film with three-dimensional structure prepared by hydrothermal process for supercapacitor, Journal of Power Sources 199 (2012) 409-412.
[36] T.K.A. Hoang, M. Acton, H.T.H. Chen, Y. Huang, T.N.L. Doan, P. Chen, Sustainable gel electrolyte containing Pb^{2+} as corrosion inhibitor and dendrite suppressor for the zinc anode in the rechargeable hybrid aqueous battery, Materials Today Energy 4 (2017) 34-40.
[37] N. Tang, X. Tian, C. Yang, Z. Pi, Q. Han, Facile synthesis of α-MnO2 nanorods for high-performance alkaline batteries, Journal of Physics and Chemistry of Solids 71 (2010) 258-262.
[38] G.Q. Zhang, X.G. Zhang, A novel alkaline Zn/MnO2 cell with alkaline solid polymer electrolyte, Solid State Ionics 160 (2003) 155-159.
[39] K.W. Pratt, W.F. Koch, Y.C. Wu, P.A. Berezansky, in: Pure and Applied Chemistry, 2001, pp. 1783.

[40] R. Younesi, G.M. Veith, P. Johansson, K. Edström, T. Vegge, Lithium salts for advanced lithium batteries: Li–metal, Li–O_2, and Li–S, Energy Environ. Sci. 8 (2015) 1905-1922.
[41] A. Ghosh, C. Wang, P. Kofinas, Block Copolymer Solid Battery Electrolyte with High Li-Ion Transference Number, Journal of The Electrochemical Society 157 (2010) A846-A849.
[42] X. Zheng, Y. Chen, X. Zheng, G. Zhao, K. Rui, P. Li, X. Xu, Z. Cheng, S.X. Dou, W. Sun, Electronic Structure Engineering of LiCoO2 toward Enhanced Oxygen Electrocatalysis, Advanced Energy Materials 0 (2019) 1803482.
[43] J. Zheng, G. Tan, P. Shan, T. Liu, J. Hu, Y. Feng, L. Yang, M. Zhang, Z. Chen, Y. Lin, J. Lu, J.C. Neuefeind, Y. Ren, K. Amine, L.-W. Wang, K. Xu, F. Pan, Understanding Thermodynamic and Kinetic Contributions in Expanding the Stability Window of Aqueous Electrolytes, Chem 4 (2018) 2872-2882.
[44] T. Biswick, W. Jones, A. Pacuła, E. Serwicka, J. Podobinski, Evidence for the formation of anhydrous zinc acetate and acetic anhydride during the thermal degradation of zinc hydroxy acetate, Zn5(OH)8(CH3CO2)2·4H2O to ZnO, Solid State Sciences 11 (2009) 330-335.
[45] J.-Y. Luo, W.-J. Cui, P. He, Y.-Y. Xia, Raising the cycling stability of aqueous lithium-ion batteries by eliminating oxygen in the electrolyte, Nature Chemistry 2 (2010) 760.
[46] C.-C. Yang, S.-J. Lin, Improvement of high-rate capability of alkaline Zn–MnO_2 battery, Journal of Power Sources 112 (2002) 174-183.
[47] F. Wang, O. Borodin, T. Gao, X. Fan, W. Sun, F. Han, A. Faraone, J.A. Dura, K. Xu, C. Wang, Highly reversible zinc metal anode for aqueous batteries, Nature Materials 17 (2018) 543-549.
[48] J. Zhao, J. Zhang, W. Yang, B. Chen, Z. Zhao, H. Qiu, S. Dong, X. Zhou, G. Cui, L. Chen, "Water-in-deep eutectic solvent" electrolytes enable zinc metal anodes for rechargeable aqueous batteries, Nano Energy 57 (2019) 625-634.
[49] Q.C. Horn, Y. Shao-Horn, Morphology and Spatial Distribution of ZnO Formed in Discharged Alkaline Zn/MnO[sub 2] AA Cells, Journal of The Electrochemical Society 150 (2003) A652.
[50] A.R.S. Kannan, S. Muralidharan, K.B. Sarangapani, V. Balaramachandran, V. Kapali, Corrosion and anodic behaviour of zinc and its ternary alloys in alkaline battery electrolytes, Journal of Power Sources 57 (1995) 93-98.
[51] J. Huang, G.G. Yadav, J.W. Gallaway, X. Wei, M. Nyce, S. Banerjee, A calcium hydroxide interlayer as a selective separator for rechargeable alkaline Zn/MnO2 batteries, Electrochemistry Communications 81 (2017) 136-140.
[52] T. Zhou, W. Lv, J. Li, G. Zhou, Y. Zhao, S. Fan, B. Liu, B. Li, F. Kang, Q.-H. Yang, Twinborn TiO_2–TiN heterostructures enabling smooth trapping–diffusion–conversion of polysulfides towards ultralong life lithium–sulfur batteries, Energy Environ. Sci. 10 (2017) 1694-1703.
[53] N. Zhang, F. Cheng, Y. Liu, Q. Zhao, K. Lei, C. Chen, X. Liu, J. Chen, Cation-Deficient Spinel ZnMn2O4 Cathode in Zn(CF3SO3)2 Electrolyte for Rechargeable Aqueous Zn-Ion Battery, Journal of the American Chemical Society 138 (2016) 12894-12901.
[54] L. Chen, Q. Gu, X. Zhou, S. Lee, Y. Xia, Z. Liu, New-concept batteries based on aqueous Li^+/Na^+ mixed-ion electrolytes, Scientific Reports 3 (2013) 1946.
[55] Y.G. Guo, J.S. Hu, L.J. Wan, Nanostructured materials for electrochemical energy conversion and storage devices, Advanced Materials 20 (2008) 2878-2887.
[56] J. Maier, Nanoionics: ion transport and electrochemical storage in confined systems, Nature Materials 4 (2005) 805-815.
[57] W.J. Wruck, B. Reichman, K.R. Bullock, W.H. Kao, Rechargeable Zn - MnO_2 alkaline batteries, Journal of the Electrochemical Society 138 (1991) 3560-3567.
[58] M. Liu, Q. Zhao, H. Liu, J. Yang, X. Chen, L. Yang, Y. Cui, W. Huang, W. Zhao, A. Song, Y. Wang, S. Ding, Y. Song, G. Qian, H. Chen, F. Pan, Tuning phase evolution of β-MnO_2 during microwave hydrothermal synthesis for high-performance aqueous Zn ion battery, Nano Energy 64 (2019) 103942.
[59] M.H. Alfaruqi, V. Mathew, J. Gim, S. Kim, J. Song, J.P. Baboo, S.H. Choi, J. Kim, Electrochemically induced structural transformation in a γ-MnO_2 cathode of a high capacity zinc-ion battery system, Chemistry of Materials 27 (2015) 3609-3620.

[60] D.L. Chao, W.H. Zhou, C. Ye, Q.H. Zhang, Y.G. Chen, L. Gu, K. Davey, S.Z. Qiao, An electrolytic Zn-MnO_2 battery for high-voltage and scalable energy storage, Angewandte Chemie-International Edition 58 (2019) 7823-7828.
[61] P.K. Sharma, M.S. Whittingham, The role of tetraethyl ammonium hydroxide on the phase determination and electrical properties of γ-MnOOH synthesized by hydrothermal, Materials Letters 48 (2001) 319-323.
[62] T. Kohler, T. Armbruster, E. Libowitzky, Hydrogen Bonding and Jahn–Teller Distortion in Groutite,α-MnOOH, and Manganite,γ-MnOOH, and Their Relations to the Manganese Dioxides Ramsdellite and Pyrolusite, Journal of Solid State Chemistry 133 (1997) 486-500.
[63] H. Pan, Y. Shao, P. Yan, Y. Cheng, K.S. Han, Z. Nie, C. Wang, J. Yang, X. Li, P. Bhattacharya, K.T. Mueller, J. Liu, Reversible aqueous zinc/manganese oxide energy storage from conversion reactions, Nature Energy 1 (2016) 16039.
[64] G. Kettlgruber, M. Kaltenbrunner, C.M. Siket, R. Moser, I.M. Graz, R. Schwödiauer, S. Bauer, Intrinsically stretchable and rechargeable batteries for self-powered stretchable electronics, Journal of Materials Chemistry A 1 (2013) 5505-5508.
[65] X. Yu, Y. Fu, X. Cai, H. Kafafy, H. Wu, M. Peng, S. Hou, Z. Lv, S. Ye, D. Zou, Flexible fiber-type zinc–carbon battery based on carbon fiber electrodes, Nano Energy 2 (2013) 1242-1248.
[66] Y. Huang, W. He, P. Zhang, X. Lu, Nitrogen-doped MnO2 nanorods as cathodes for high-energy Zn-MnO2 batteries, Functional Materials Letters 11 (2018) 1840006.
[67] Y. Jin, L. Zou, L. Liu, M.H. Engelhard, R.L. Patel, Z. Nie, K.S. Han, Y. Shao, C. Wang, J. Zhu, H. Pan, J. Liu, Joint Charge Storage for High-Rate Aqueous Zinc–Manganese Dioxide Batteries, Advanced Materials 31 (2019) 1900567.
[68] M. Chamoun, W.R. Brant, C.-W. Tai, G. Karlsson, D. Noréus, Rechargeability of aqueous sulfate Zn/MnO2 batteries enhanced by accessible Mn2+ ions, Energy Storage Materials 15 (2018) 351-360.
[69] Z. Liu, D. Wang, Z. Tang, G. Liang, Q. Yang, H. Li, L. Ma, F. Mo, C. Zhi, A mechanically durable and device-level tough Zn-MnO2 battery with high flexibility, Energy Storage Materials 23 (2019) 636-645.
[70] D. Lin, Y. Liu, Y. Cui, Reviving the lithium metal anode for high-energy batteries, Nature Nanotechnology 12 (2017) 194-206.

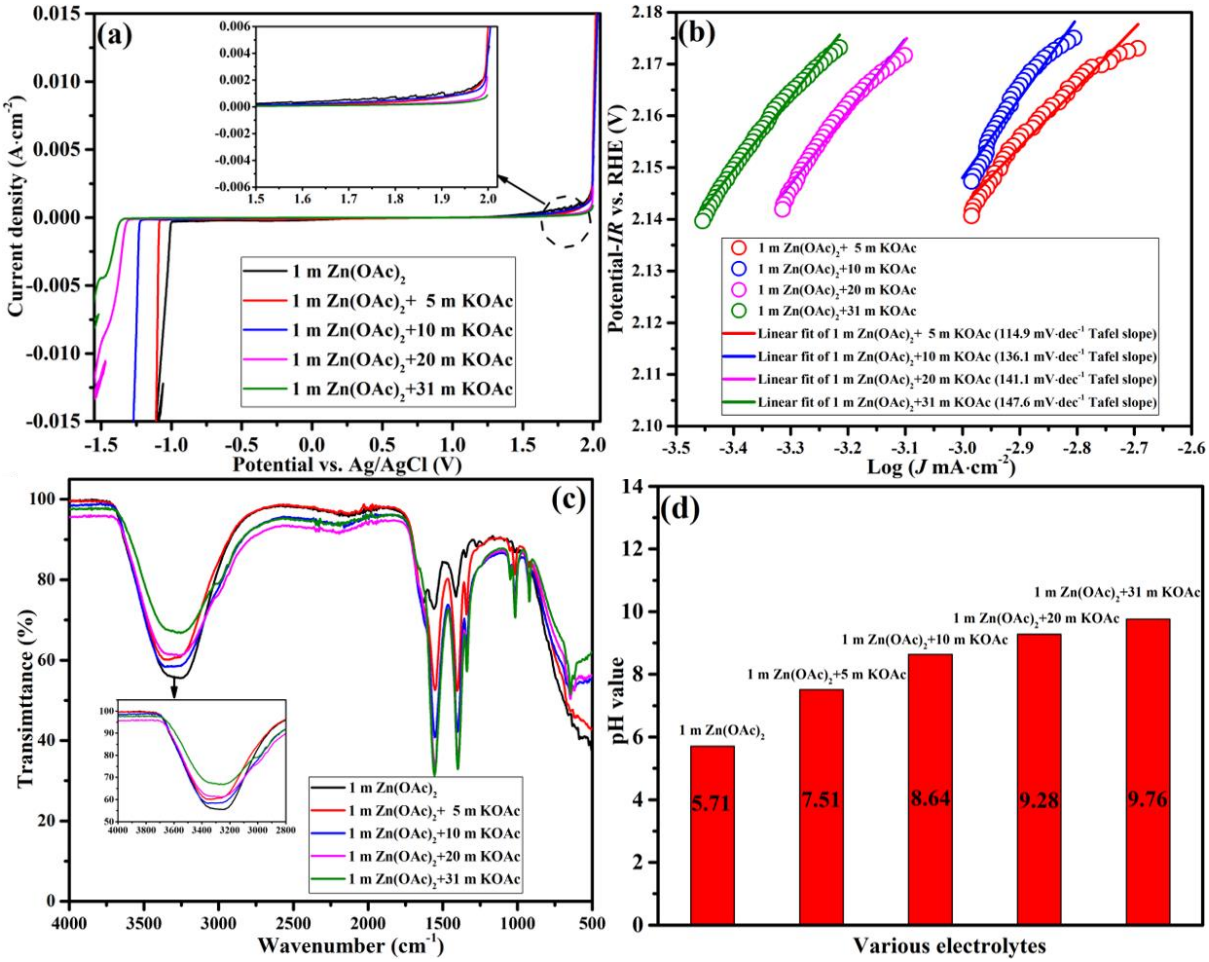

Fig. 1. (a) Stability window test on the acetate-based salt-concentrated electrolytes under 1 mV·s^{-1} scanning rate. (b) Tafel curves of acetate-based salt-concentrated electrolytes regarding OER. (c) FTIR spectra of the acetate-based salt-concentrated electrolytes. (d) pH value of the acetate-based salt-concentrated electrolytes at room temperature.

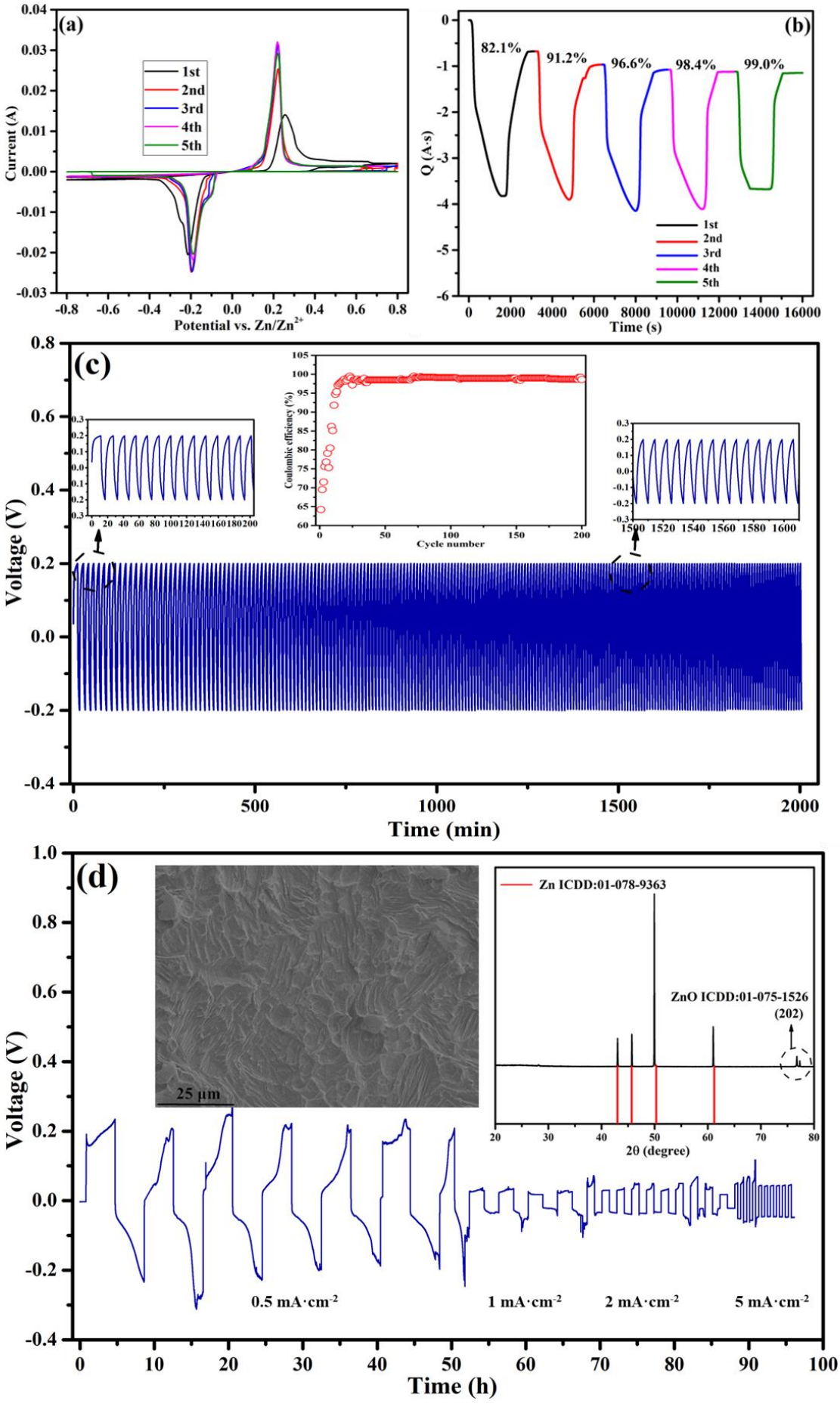
(a)
1st
2nd
3rd
4th
5th
Current (A)
Potential vs. Zn/Zn2+
(b)
82.1%
91.2%
96.6%
98.4%
99.0%
Q (A·s)
Time (s)
(c)
Coulombic efficiency (%)
Cycle number
Voltage (V)
Time (min)
(d)
25 μm
Zn ICDD:01-078-9363
ZnO ICDD:01-075-1526
(202)
2θ (degree)
0.5 mA·cm-2
1 mA·cm-2
2 mA·cm-2
5 mA·cm-2
Voltage (V)
Time (h)

Fig. 2. (a) CV curves of Zn plating/stripping in Zn/Ti cell under 1 $mV \cdot s^{-1}$ scanning rate. (b) Chronocoulometry curves derived from the CV curves of that Zn/Ti coin cell. (c) Galvanostatic Zn stripping/plating in a Zn/Zn symmetrical cell under 5 $mA \cdot cm^{-2}$ current density with -0.2 to 0.2 voltage limitation. (d) Galvanostatic Zn stripping/plating in a Zn/Zn symmetrical cell under 0.5, 1, 2 and 5 $mA \cdot cm^{-2}$ current density with 2 $mAh \cdot cm^{-2}$ capacity limitation.

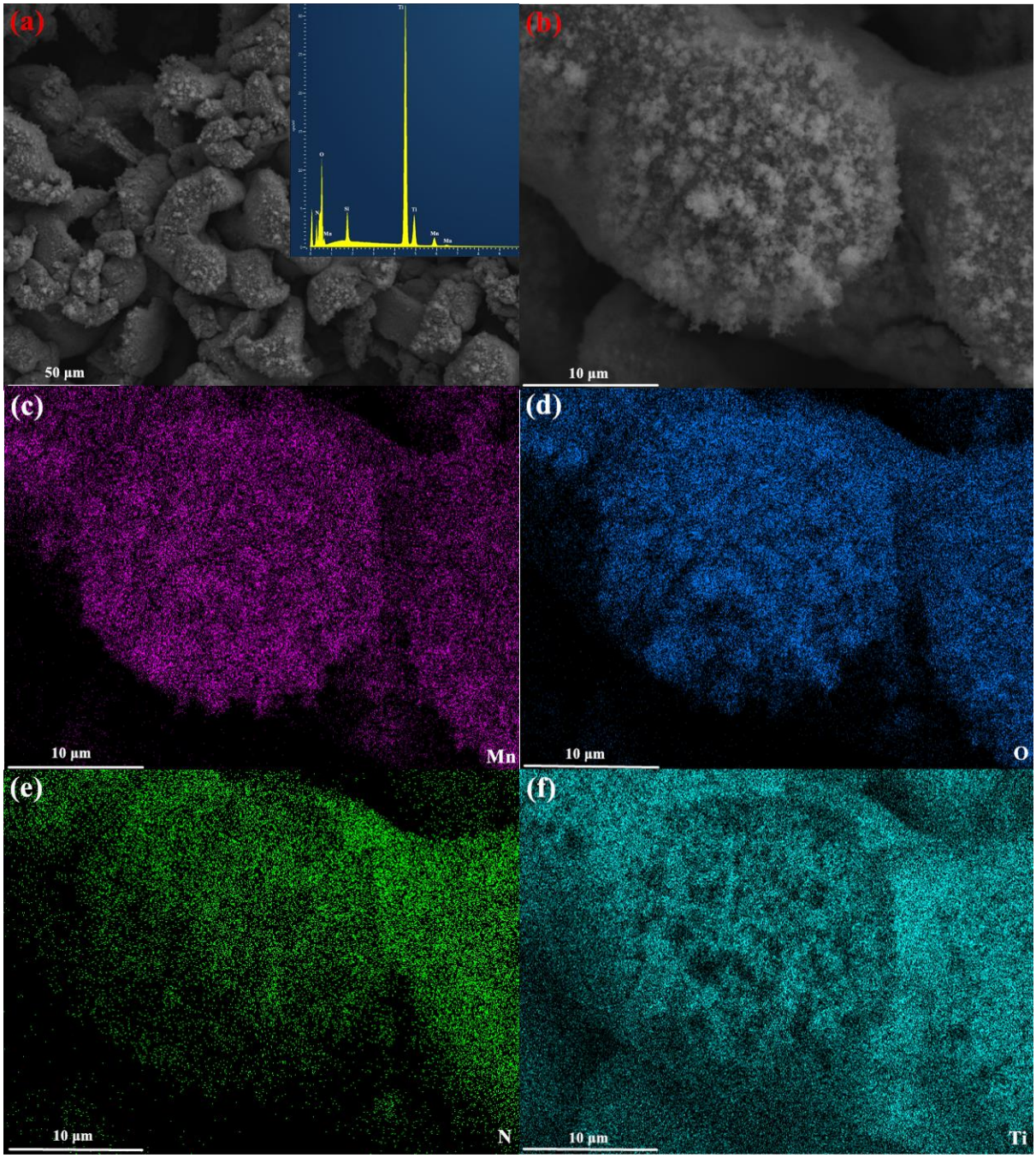

Fig. 3. (a) SEM image of self-supported MnO_2-TiN/TiO_2 cathode under 50 μm resolution with EDX element analysis as inset. (b) SEM images of self-supported MnO_2-TiN/TiO_2 cathode under 10 μm resolution and according EDX mappings of (c) Mn, (d) O and (e) N and (f) Ti elements.

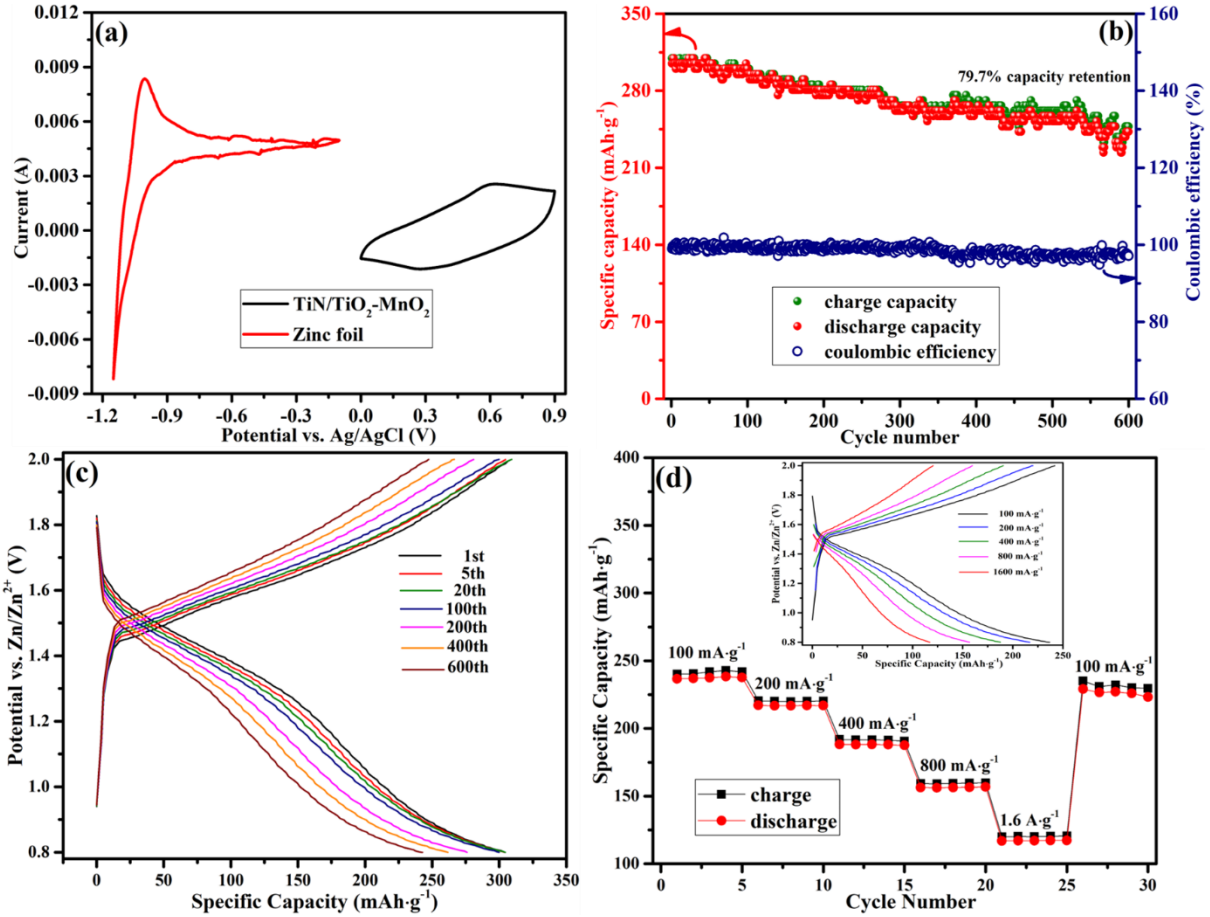

Fig. 4. (a) CV curves of Zn and MnO_2-TiN/TiO_2 cathode with Ti foil as counter electrode and Ag/AgCl as reference. (b) Cyclic performance of Zn/MnO_2 full cell under 100 mA·g^{-1} current density between 0.8 and 2.0 versus Zn/Zn^{2+} within 600 cycles. (c) Charge-discharge curves of Zn/MnO_2 full cell between 0.8 and 2.0 V versus Zn/Zn^{2+} of 1st, 5th, 20th, 100th, 200th, 400th and 600th cycles. (d) Rate performance of Zn/MnO_2 full cell under 100, 200, 400, 800 and 1600 mA·g^{-1} current density with the according charge-discharge curves shown in the inset.

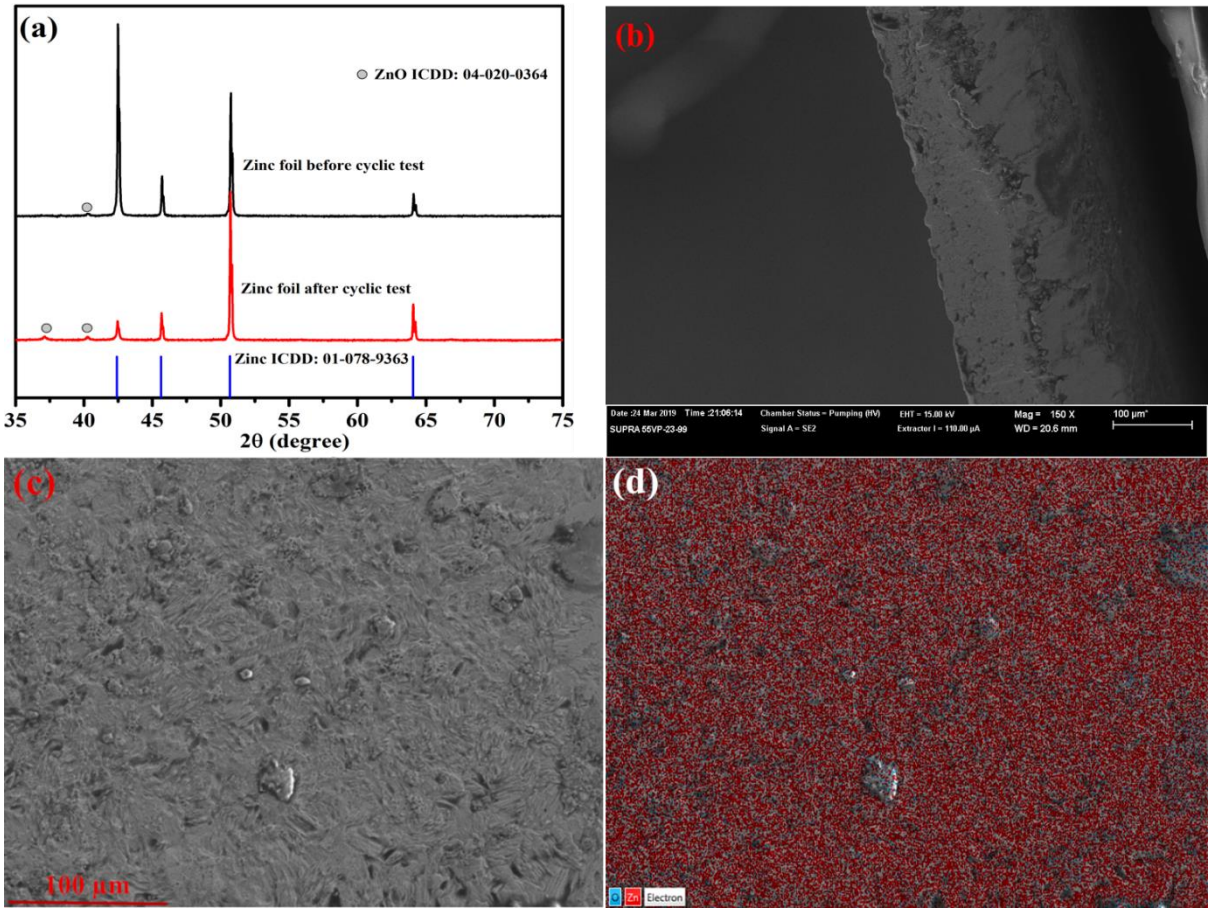

Fig. 5. (a) XRD on the Zn anodes before and after cyclic test. (b) SEM image about the cross section of Zn anode after cyclic test. (c) SEM image on the surface and (d) corresponding layer mapping of Zn and O elements on Zn foil anode after cyclic test.

Supporting Information

Salt-concentrated acetate electrolytes for a high voltage aqueous Zn/MnO_2 battery

*Shigang Chen [a], Rong Lan [a,c] John Humphreys [a] and Shanwen Tao [a,b]**

[a] *School of Engineering, University of Warwick, Coventry CV4 7AL, UK*
[b] *Department of Chemical Engineering, Monash University, Clayton, Victoria 3800, Australia*
[c] *Faculty of Engineering, Environment & Computing, Coventry University, Coventry, CV1 5FB, UK*

Table S1. Summary on electrochemical windows and ionic conductivity of various electrolytes.

Sample	Electrochemical window (vs. Ag/AgCl) at 1 $mV \cdot s^{-1}$ (V)	Ionic conductivity ($S \cdot cm^{-1}$)
1 m $Zn(OAc)_2$	-1 to 1.6	1.53×10^{-2}
1 m $Zn(OAc)_2$+5 m KOAc	-1.1 to 1.7	1.01×10^{-1}
1 m $Zn(OAc)_2$+10 m KOAc	-1.3 to 1.7	9.70×10^{-2}
1 m $Zn(OAc)_2$+20 m KOAc	-1.4 to 1.95	5.29×10^{-2}
1 m $Zn(OAc)_2$+31 m KOAc	-1.45 to 1.95	2.96×10^{-2}

Table S2. Comparison of the performance of some recent works on Zn/MnO_2 batteries calculation by different methods.

Anode Material	Cathode Material	Electrolyte Material	Voltage limitation	Capacity	Energy density	References
Zn powder-Zn foil	MnO_2 powder-carbon paper	2 M $ZnSO_4$ + 0.1 M $MnSO_4$ aqueous electrolyte	1.0 to 1.8 V vs. Zn/Zn^{2+}	233 $mAh \cdot g^{-1}$ (under 1 C, based on the mass of MnO_2)	N/A	Energy Storage Materials, 2018, 15, 351.
Zn nanosheet-CNT paper	MnO_2 nanorods-CNT paper	2M $ZnSO_4$+0.1 M MnSO4-Zn-alginate/PAAm hydrogel electrolyte	0.9 to 1.8 V vs. Zn/Zn^{2+}	300.4 $mAh \cdot g^{-1}$ (under 0.11 $A \cdot g^{-1}$ current density, based on the mass of MnO_2)	N/A	Energy Storage Materials, 2019, 23, 636.
Zn metal plate	β-MnO_2/Bi_2O_3 powder-Ni mesh	1 M KOH + 3 M LiOH aqueous electrolyte	-1.0 to 0.1 V vs. Hg/HgO	360 $mAh \cdot g^{-1}$ (under 1 C, based on the mass of MnO_2)	N/A	Chemistry of Materials, 2016, 28, 4536.
Zinc foil	δ-MnO_2 powder-carbon paper	1 M $Zn(TFSI)_2$+0.1 M $Mn(TFSI)_2$ aqueous electrolyte	1.0 to 1.8 V vs. Zn/Zn^{2+}	136.9 $mAh \cdot g^{-1}$ (under 20 C, based on the mass of MnO_2)	N/A	Advanced Materials, 2019, 31, 1900567.
Zn nanosheet-carbon cloth	MnO_2@PEDOT-carbon cloth	3 M LiCl+2 M $ZnCl_2$+0.4 M $MnSO_4$-PVA gel electrolyte	1.0 to 1.8 V vs. Zn/Zn^{2+}	366.6 $mAh \cdot g^{-1}$ (under 0.74 $A \cdot g^{-1}$ current density, based on the mass of MnO_2)	504.9 $Wh \cdot kg^{-1}$ (based on the mass of MnO_2)	Advanced Materials, 2017, 29, 1700274.
Zn-graphite foam	MnO_2-carbon fibre cloth	1 M $ZnSO_4$+1 M $MnSO_4$+0.3 M H_2SO_4 aqueous electrolyte	0.8 to 2.0 V vs. Zn/Zn^{2+}	~570 $mAh \cdot g^{-1}$ (under 60 $mA \cdot cm^{-2}$, based on the mass of MnO_2 and Zn)	~409 $Wh \cdot kg^{-1}$ (based on the mass of MnO_2 and Zn)	Angewandte Chemie International Edition, 2019, 58, 7823.
Zn foil	N-doped MnO_2 nanorods-carbon cloth	2M $ZnSO_4$+0.4 M $MnSO_4$ aqueous electrolyte	1.0 to 1.8 V vs. Zn/Zn^{2+}	0.31 $mAh \cdot cm^{-2}$ (under 2 $mA \cdot cm^{-2}$, based on the area of electrode)	154.3$Wh \cdot kg^{-1}$ (based on the mass of MnO_2)	Functional Materials Letters, 2018, 6, 1840006

Zinc wire	MnO_2 particle-carbon fiber	$NH_4Cl+Zn(Cl)_2$ aqueous electrolyte	0.8 to 1.5 V vs. Zn/Zn^{2+}	0.29 $mAh\cdot cm^{-2}$ (under the current density of 0.15 $mA\cdot cm^{-2}$, based on the area of electrode)	0.20 $mWh\cdot cm^{-3}$ (based on the volume of MnO_2-carbon fiber electrode)	Nano Energy, 2013, 2, 1242.
Zn powder-textile mesh	MnO_2 powder-textile mesh	40 wt% KOH in purified water-CMC hydrogel electrolyte	1.0 to 1.6 V vs. Zn/Zn^{2+}	1.44 $mAh\cdot cm^{-2}$ (under the current density of 1 $mA\cdot cm^{-2}$, based on the area of electrode)	N/A	Journal of Materials Chemistry A, 2013, 1, 5505.
Zn foil	nanofiber α-MnO_2-carbon sheet	2 M $ZnSO_4$+0.1 M $MnSO_4$ aqueous electrolyte	1.0 to 1.9 V vs. Zn/Zn^{2+}	285 $mAh\cdot g^{-1}$ (under 1/3 C, based on the mass of MnO_2)	~170 $Wh\cdot kg^{-1}$ (based on the total active mass of anode, cathode and electrolyte)	Nature Energy, 2016, 1, 16039.
Zn foil	nanosized MnO_2 particle-TiN/TiO_2 porous substrate	1 m $Zn(OAc)_2$+31 m KOAc aqueous electrolyte	0.8 to 2.0 V vs. Zn/Zn^{2+}	304.6 $mAh\cdot g^{-1}$ (under 1/3 C, based on the mass of MnO_2), 0.31 $mAh\cdot cm^{-2}$ (under 0.1 $mA\cdot cm^{-2}$ current density, based on the area of electrode)	368.5 $Wh\cdot kg^{-1}$ (based on the mass of MnO_2), 232.7 $Wh\cdot kg^{-1}$ (based on the total active mass of anode, cathode and electrolyte)	This study

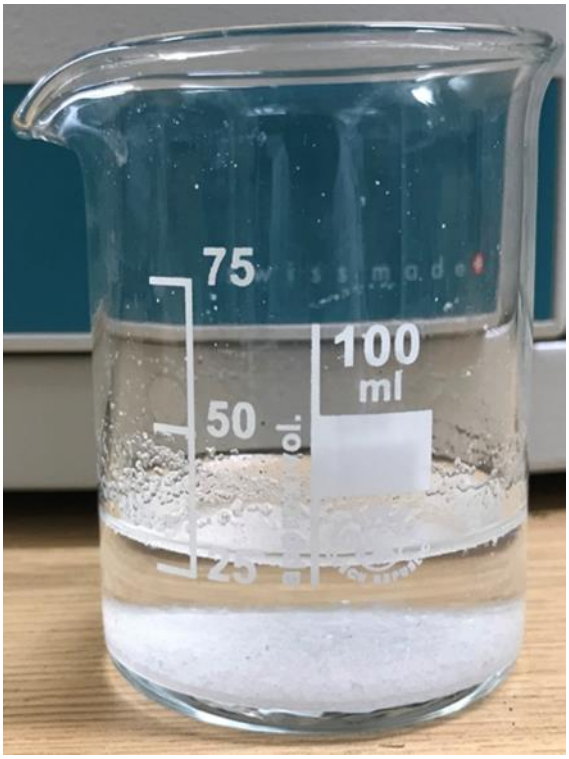

Fig. S1. The optical image of nominal 1.5 m $Zn(OAc)_2$ aqueous solution with some precipitation observed.

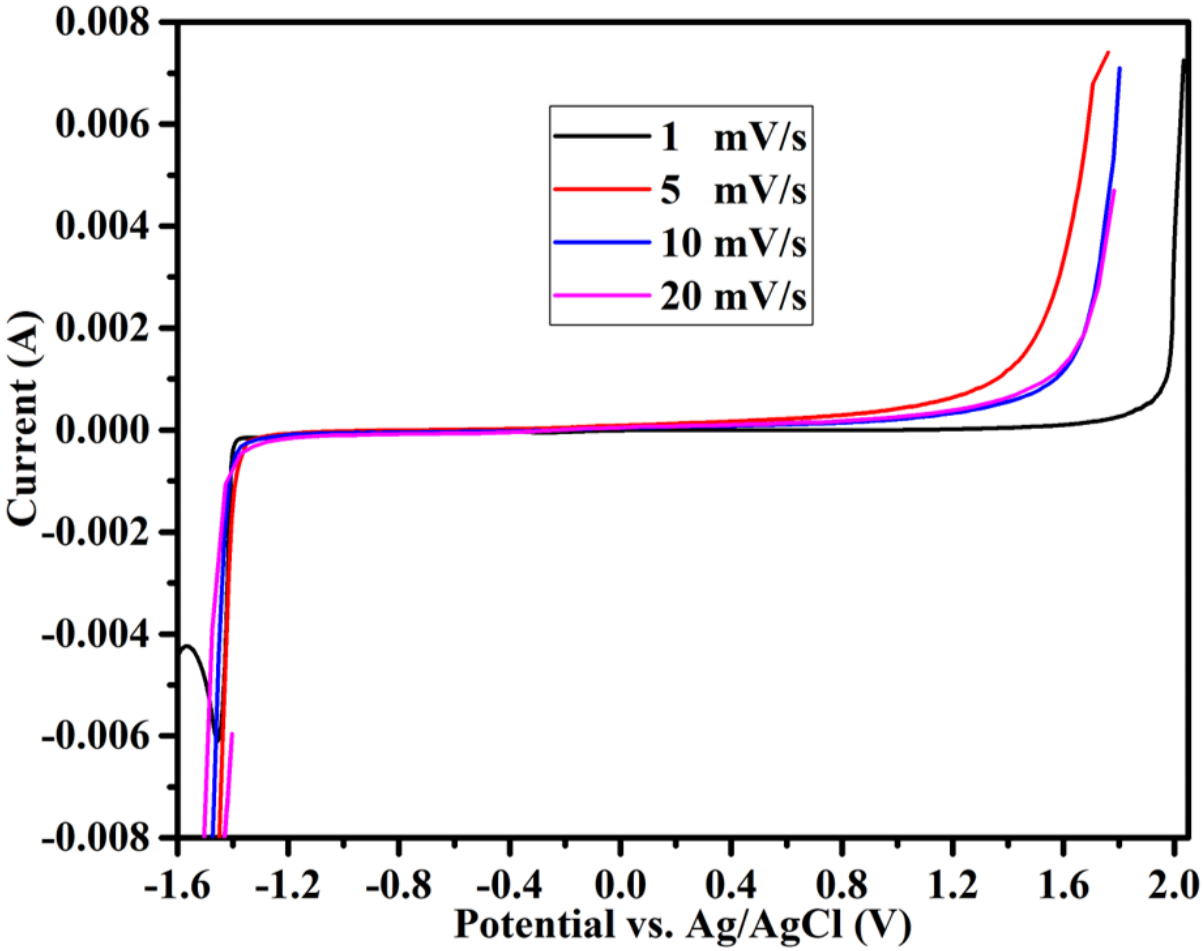

Fig. S2. The LSV curves of 1 m $Zn(OAc)_2$+31 m KOAc salt-concentrated electrolyte under various scanning rates from 1, 5, 10 to 20 $mV \cdot s^{-1}$.

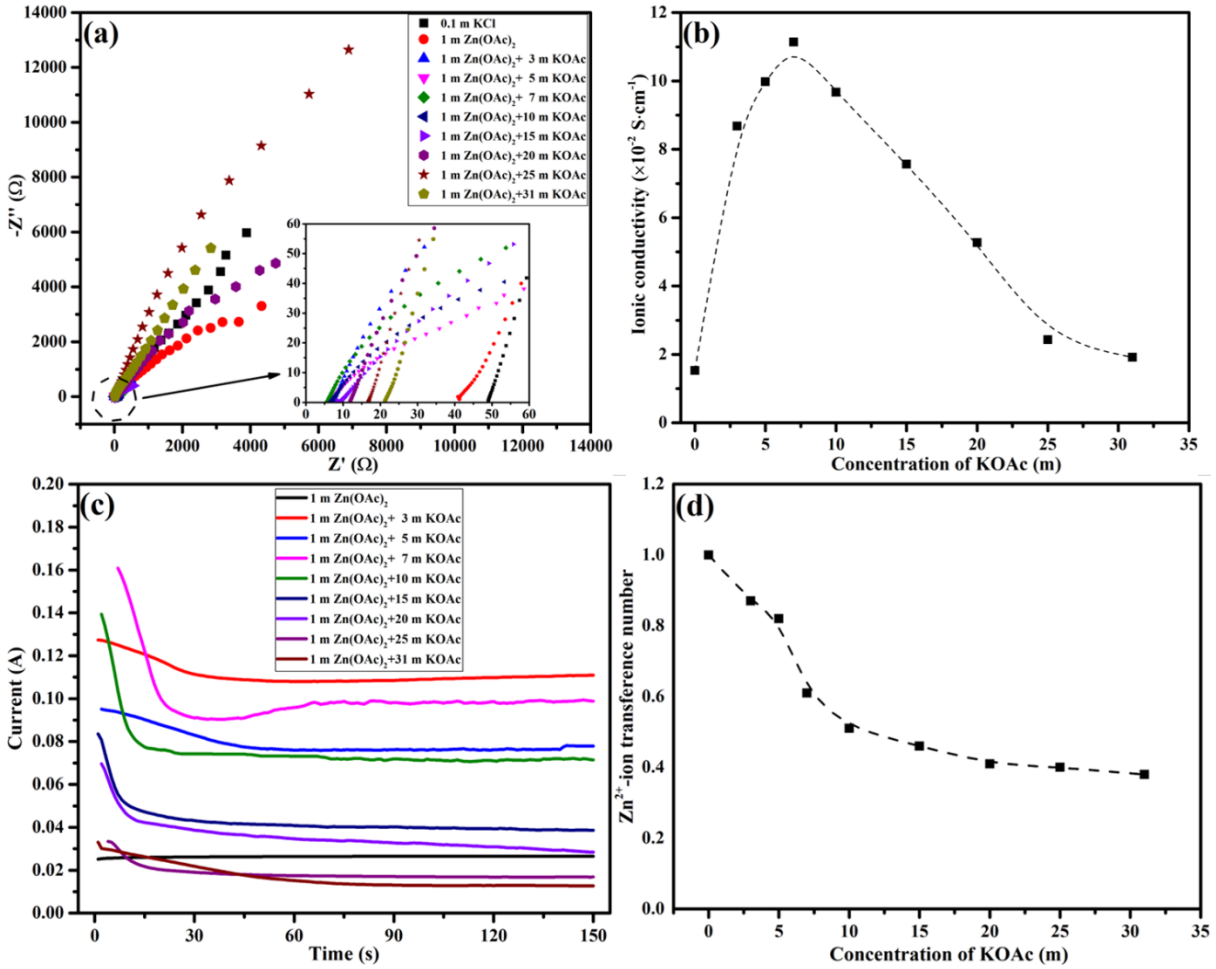

Fig. S3. (a) EIS of various electrolytes with different salt concentrations at room temperature. (b) Relationship between ionic conductivity and KOAc concentration in various electrolytes. (c) The current interrupt test on Zn/Zn symmetric cells with various electrolytes under 1 V vs. Zn/Zn^{2+} applied voltage. (d) The relationship between Zn^{2+}-ion transference number and KOAc concentration in various electrolytes.

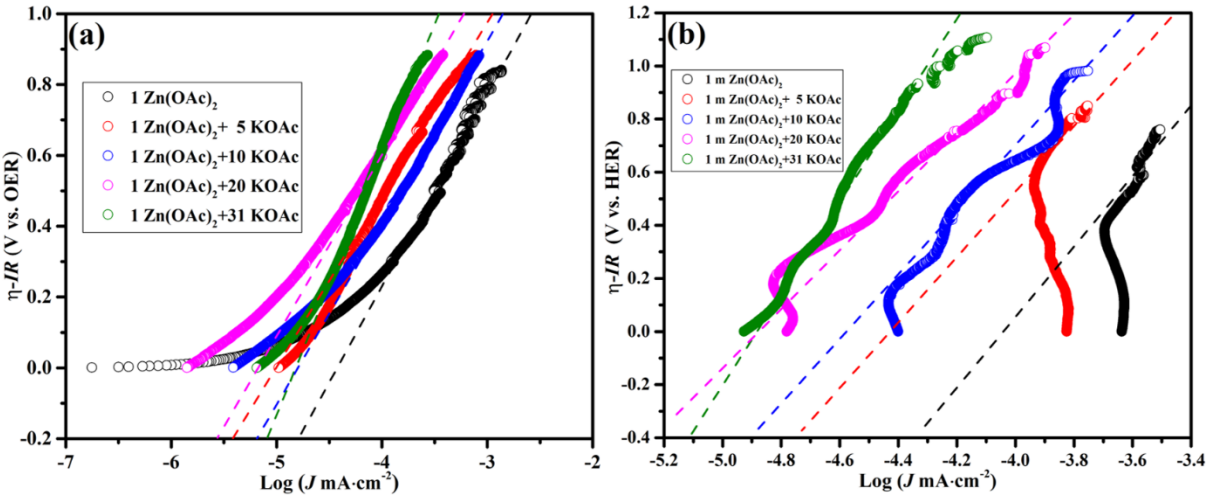

Fig. S4 (a) Tafel curves of various electrolytes in low polarization area regarding OER. (b) Tafel curves of various electrolytes in low polarization area regarding HER.

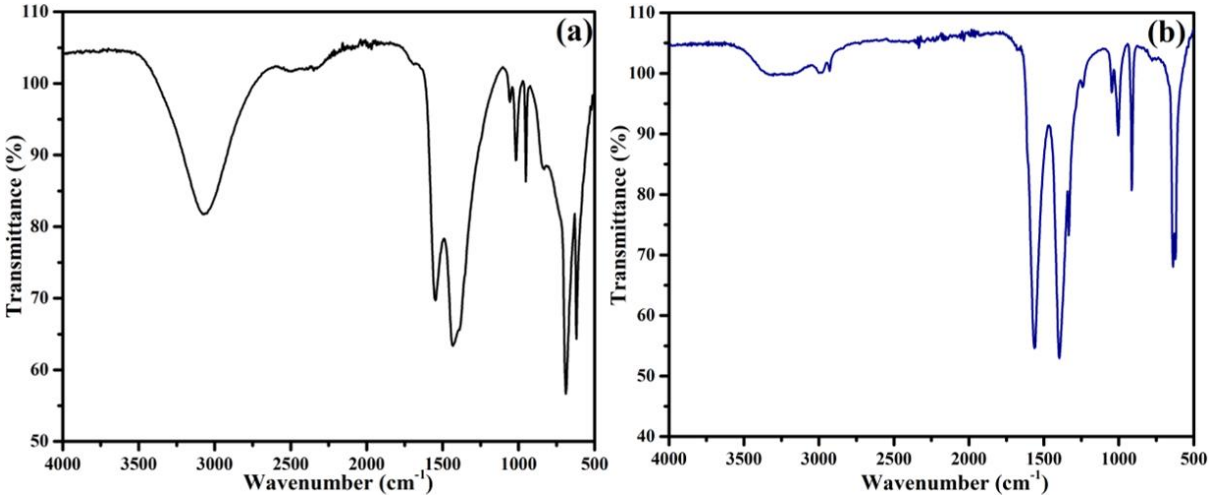

Fig. S5. (a) The FTIR spectrum of $Zn(OAc)_2 \cdot 2H_2O$ original chemical. (b) The FTIR spectrum of KOAc original chemical.

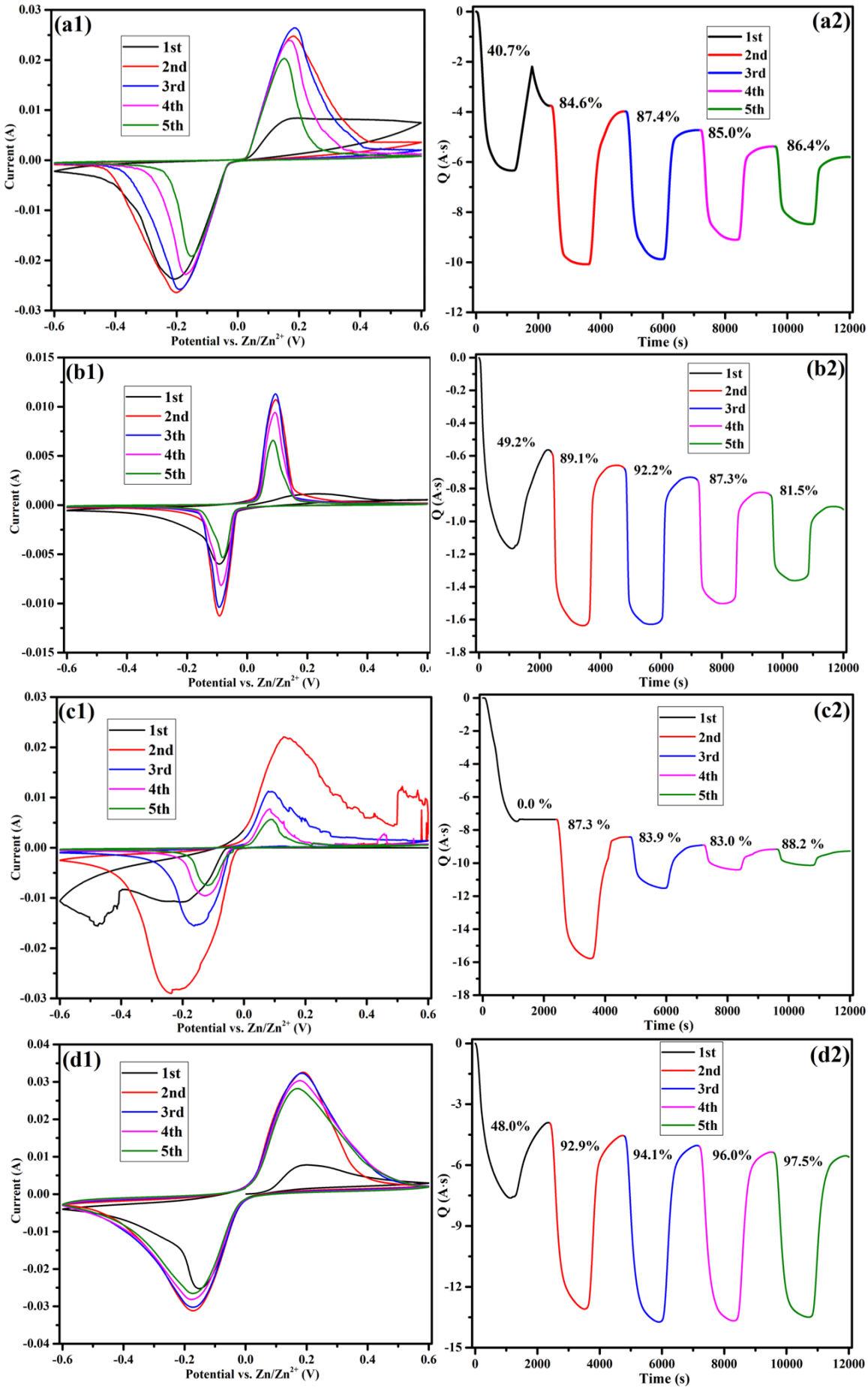
(a1)
1st
2nd
3rd
4th
5th
Current (A)
Potential vs. Zn/Zn2+ (V)
(a2)
40.7%
84.6%
87.4%
85.0%
86.4%
Q (A·s)
Time (s)
(b1)
1st
2nd
3th
4th
5th
Current (A)
Potential vs. Zn/Zn2+ (V)
(b2)
49.2%
89.1%
92.2%
87.3%
81.5%
Q (A·s)
Time (s)
(c1)
1st
2nd
3rd
4th
5th
Current (A)
Potential vs. Zn/Zn2+ (V)
(c2)
0.0 %
87.3 %
83.9 %
83.0 %
88.2 %
Q (A·s)
Time (s)
(d1)
1st
2nd
3rd
4th
5th
Current (A)
Potential vs. Zn/Zn2+ (V)
(d2)
48.0%
92.9%
94.1%
96.0%
97.5%
Q (A·s)
Time (s)

Fig.S6 (a1-d1) CV curves of Zn plating/stripping in Zn/Ti cell under 1 $mV \cdot s^{-1}$ scanning rate with 1 m $Zn(OAc)_2$, 1 m $Zn(OAc)_2$+5 m KOAc, 1 m $Zn(OAc)_2$+10 m KOAc and 1 m $Zn(OAc)_2$+20 m KOAc electrolytes respectively. (a2-d2) Chronocoulometry curves derived from the CV curves of that Zn/Ti coin cell with 1 m $Zn(OAc)_2$, 1 m $Zn(OAc)_2$+5 m KOAc, 1 m $Zn(OAc)_2$+10 m KOAc and 1 m $Zn(OAc)_2$+20 m KOAc electrolytes respectively.

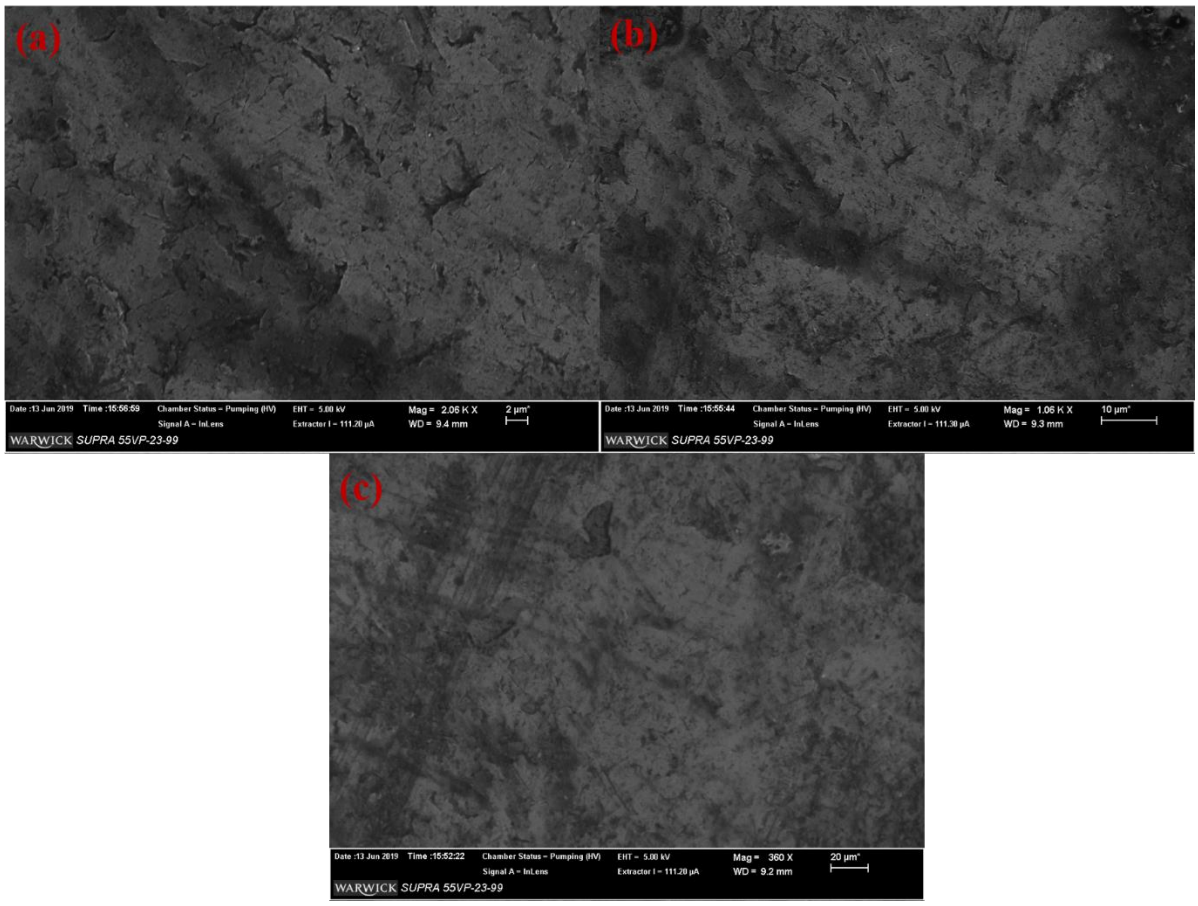

Fig. S7. (a, b, c) SEM images of Zn foil electrode of Zn/Zn symmetric cell before cyclic test with various magnifications.

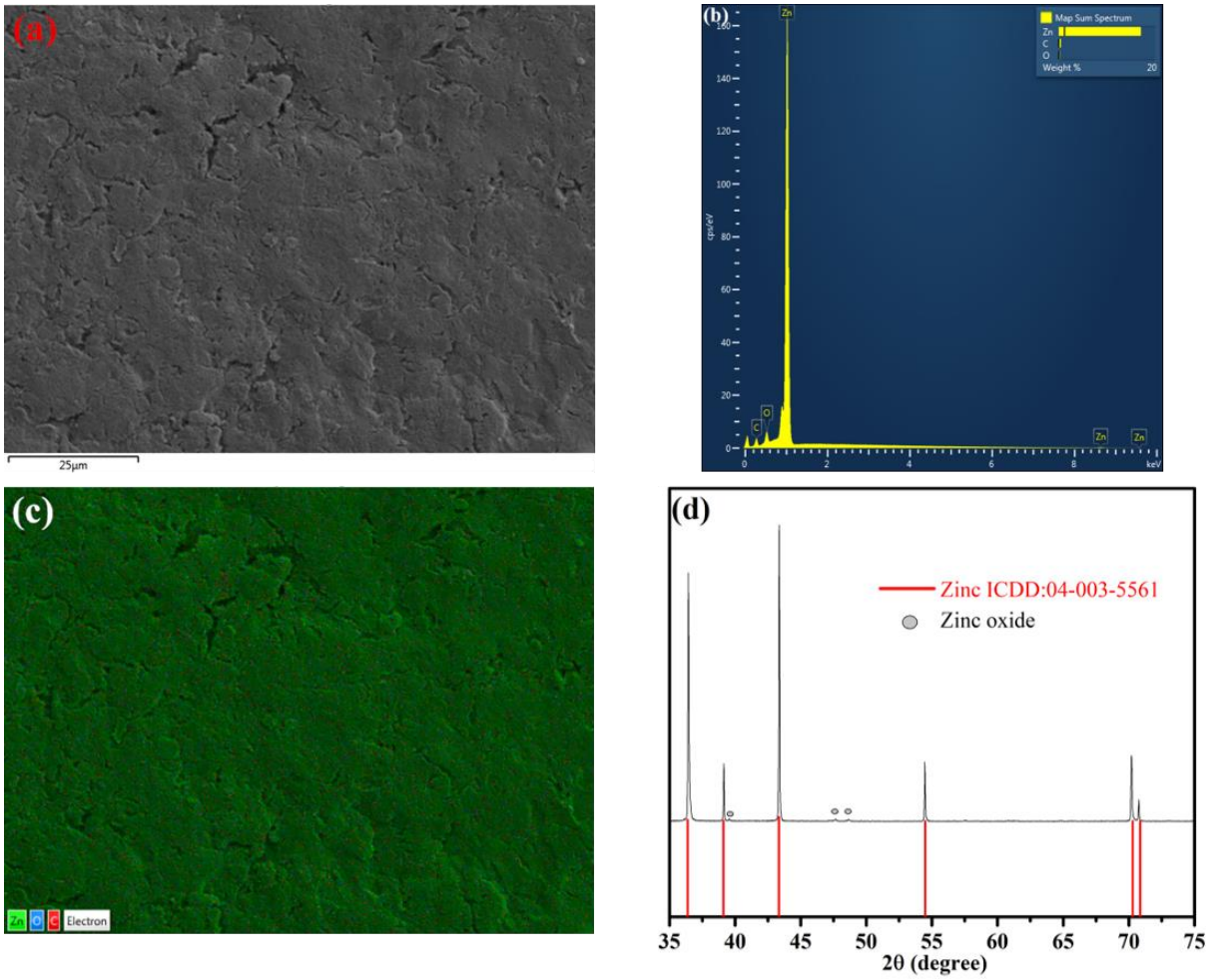

Fig. S8. (a) SEM image, (b) EDX element analysis, (c) corresponding layer mapping of Zn, O and C elements, (d) XRD analysis on Zn foil electrode of Zn/Zn symmetric cell with 1 m $Zn(OAc)_2$+31 m KOAc electrolyte after cyclic test.

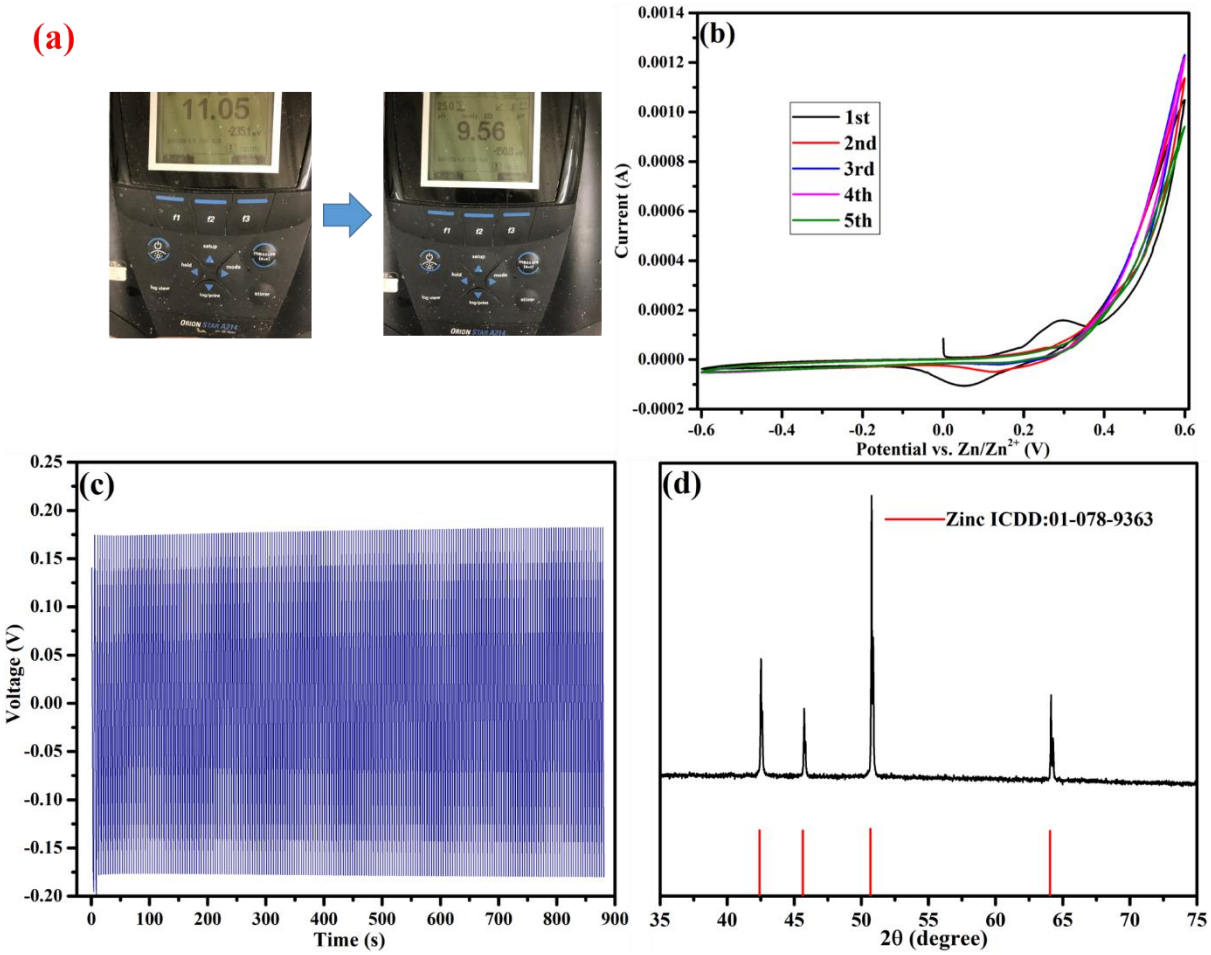

Fig. S9. (a) Optical image of pH meter when testing pH value of 31 m KOAc electrolyte before and after adjusting by acetic acid. (b) CV curves of Zn/Zn symmetrical cell with 31 m KOAc electrolyte. (c) Galvanostatic Zn stripping/plating in a Zn/Zn symmetrical cell under 0.5 $mA \cdot cm^{-2}$ current density with 31 m KOAc electrolyte. (d) XRD analysis on Zn foil electrode of Zn/Zn symmetric cell with 31 m KOAc electrolyte after cyclic test.

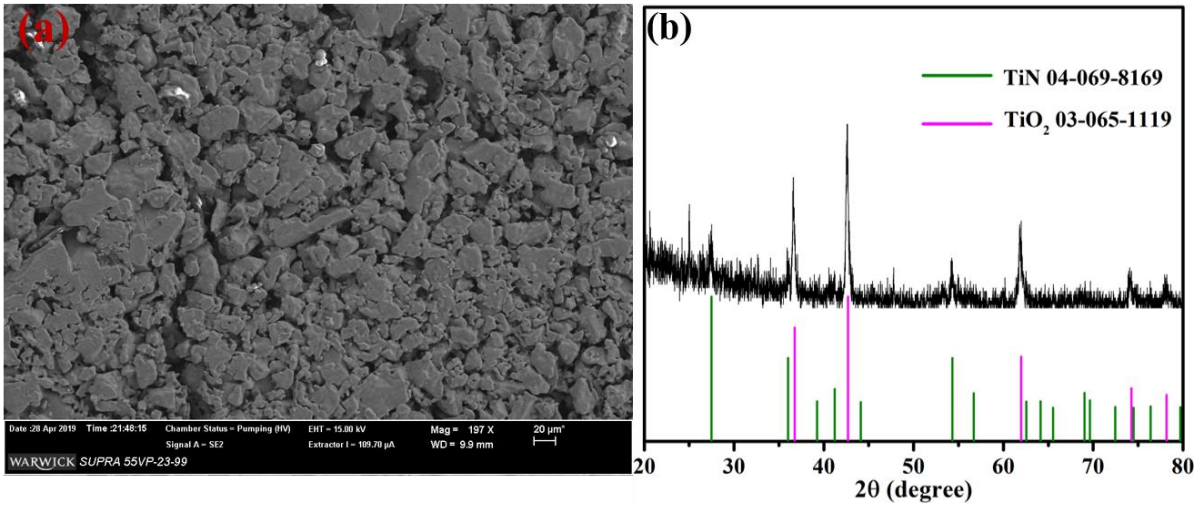

Fig. S10. (a) SEM image of TiN/TiO_2 porous substrate. (b) XRD analysis on TiN/TiO_2 porous substrate.

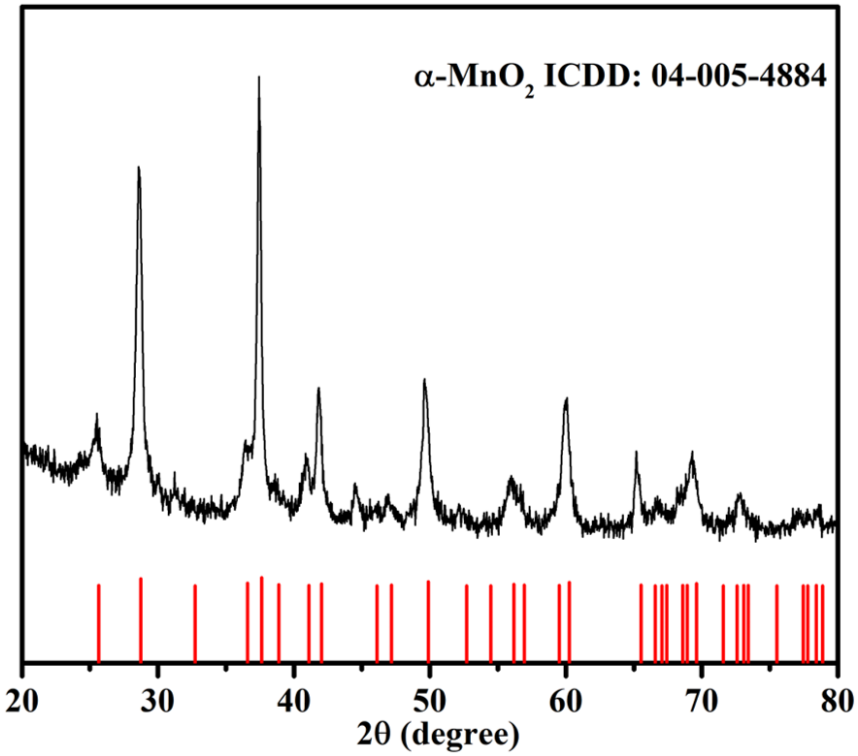

Fig. S11. XRD analysis on α-MnO_2 nanosized particles.

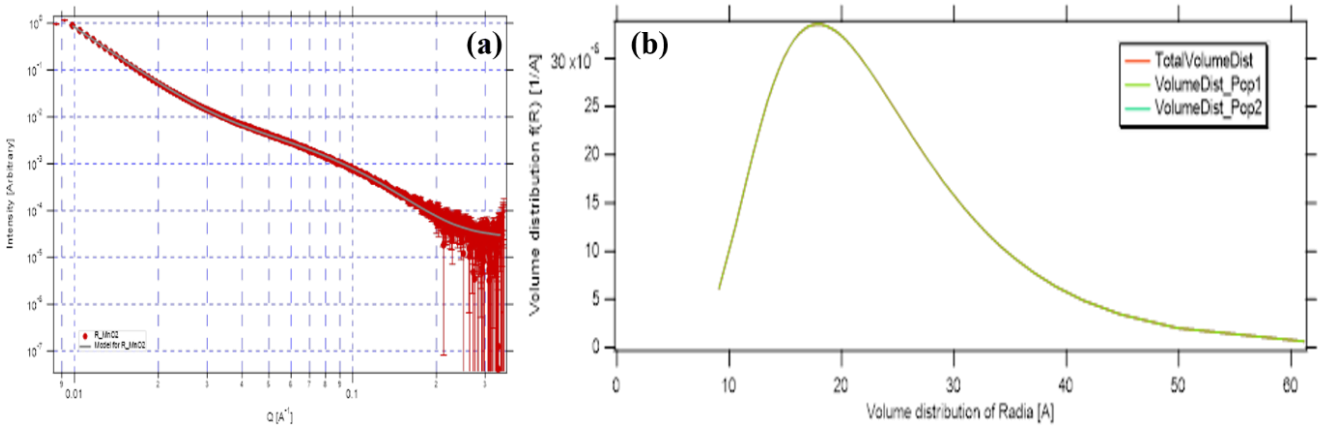

Fig. S12. SAXS analysis on α-MnO_2 nanosized particles.

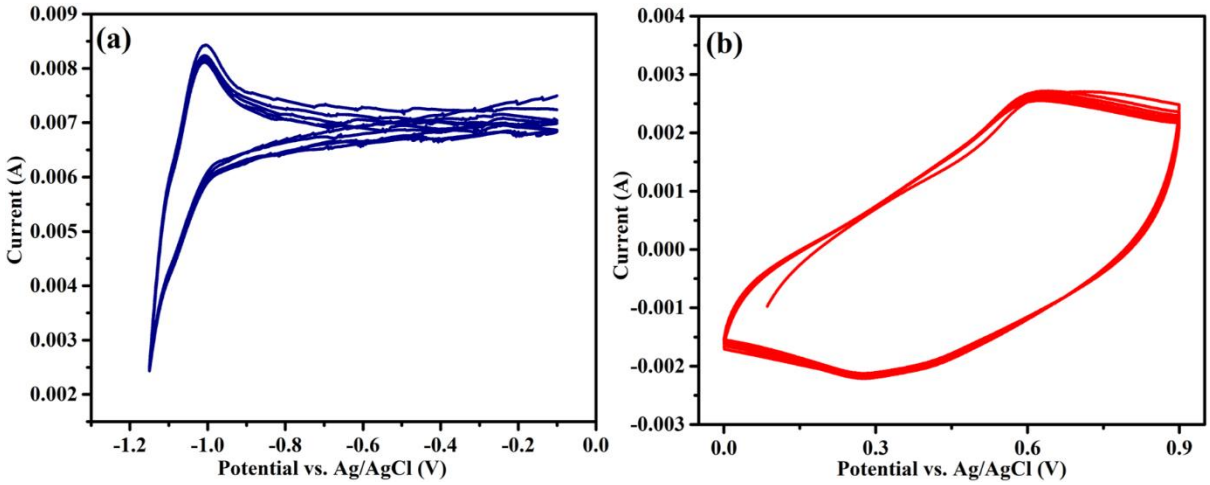

Fig. S13. (a) CV curves of Zn foil in 1 m $Zn(OAc)_2$+31 m KOAc electrolyte in three-electrode cell under 1 $mV \cdot s^{-1}$ scanning rate within 5 cycles. (b) CV curves of MnO_2-TiN/TiO_2 in 1 m $Zn(OAc)_2$+31 m KOAc electrolyte in three-electrode cell under 1 $mV \cdot s^{-1}$ scanning rate within 5 cycles.

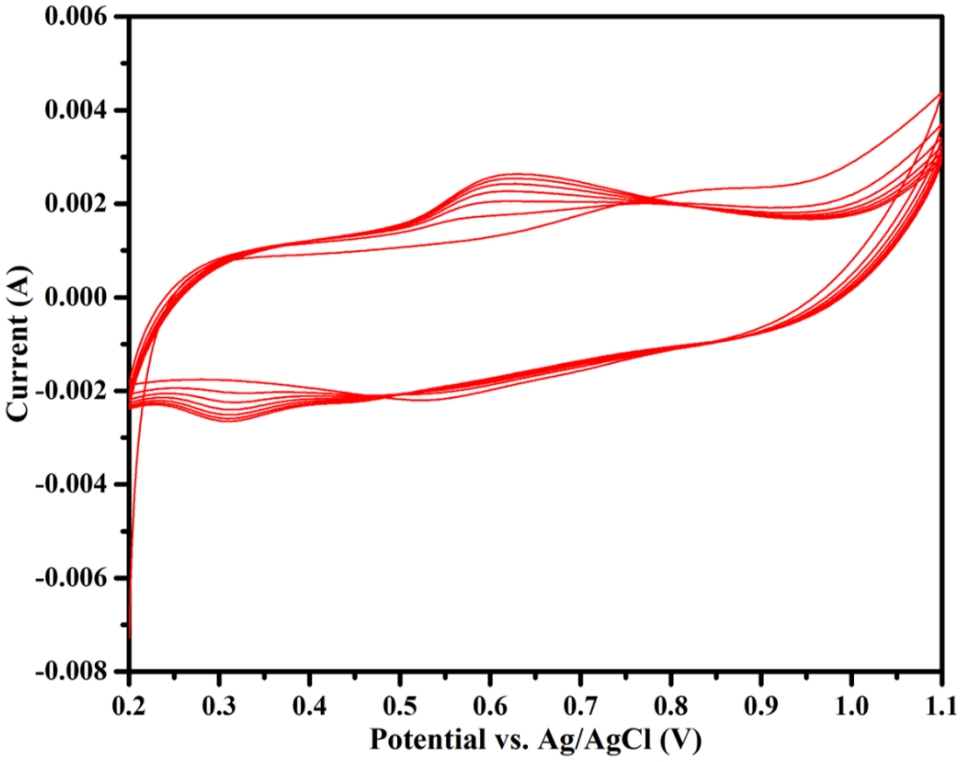

Fig. S14. CV curves of MnO_2-TiN/TiO_2 cathode in 31 m KOAc electrolyte in three-electrode cell under 1 $mV \cdot s^{-1}$ scanning rate within 5 cycles.

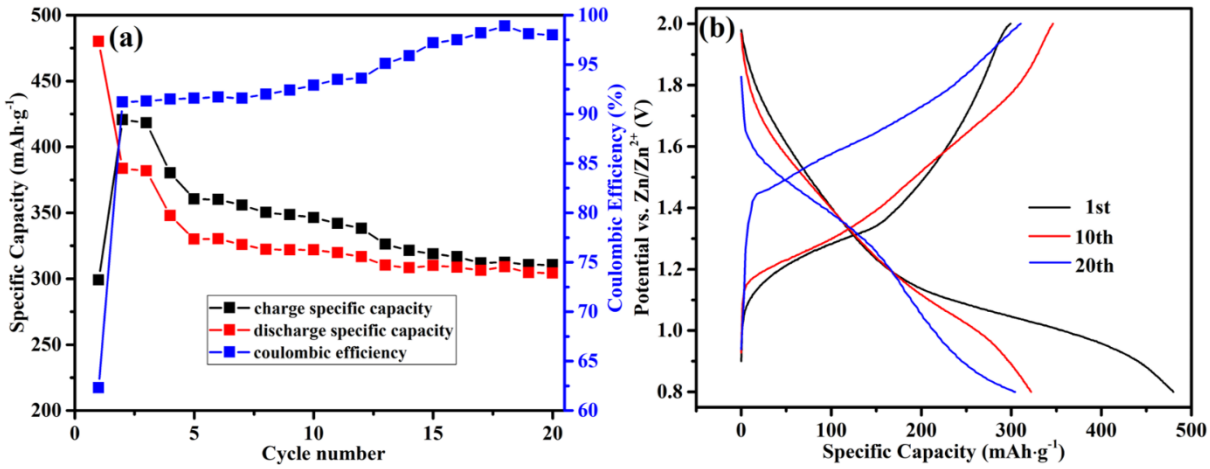

Fig. S15. (a) Charge-discharge cycling of activation on Zn/MnO_2 battery. (b) Corresponding charge-discharge curves of that Zn/MnO_2 battery.

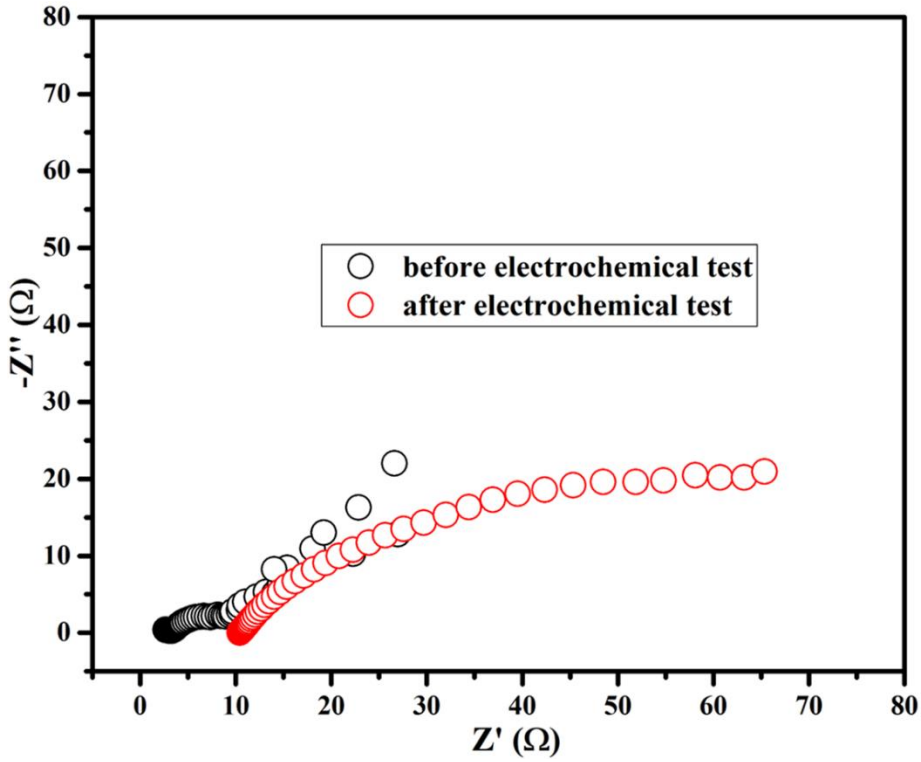

Fig. S16. EIS plot of Zn/MnO_2 coin cell before and after electrochemical test.

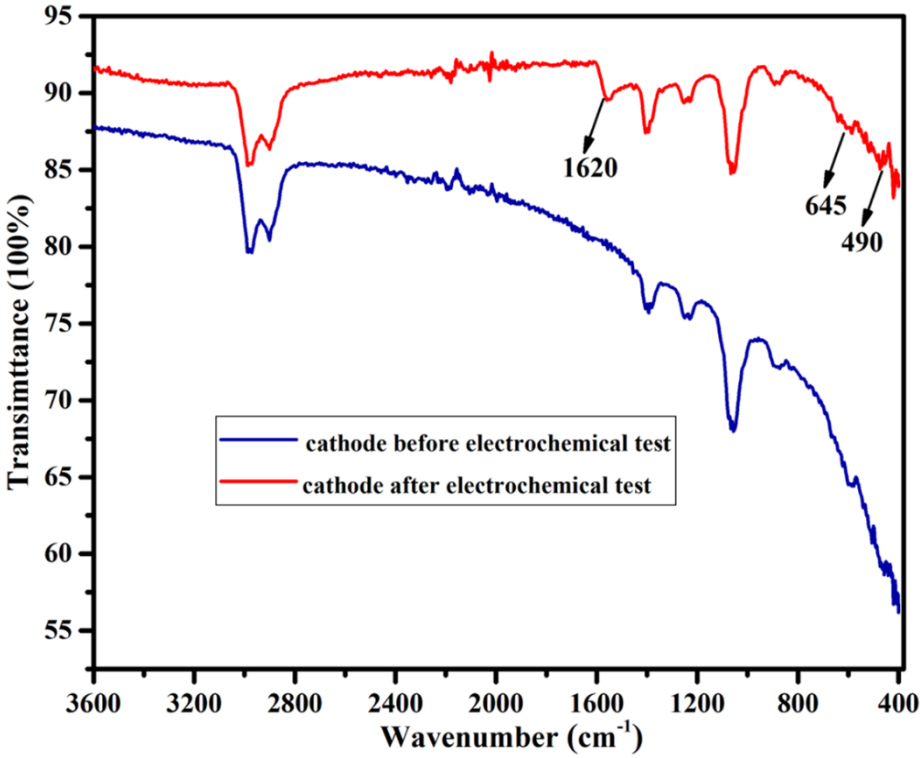

Fig. S17. FTIR spectra of cathode before and after electrochemical test.

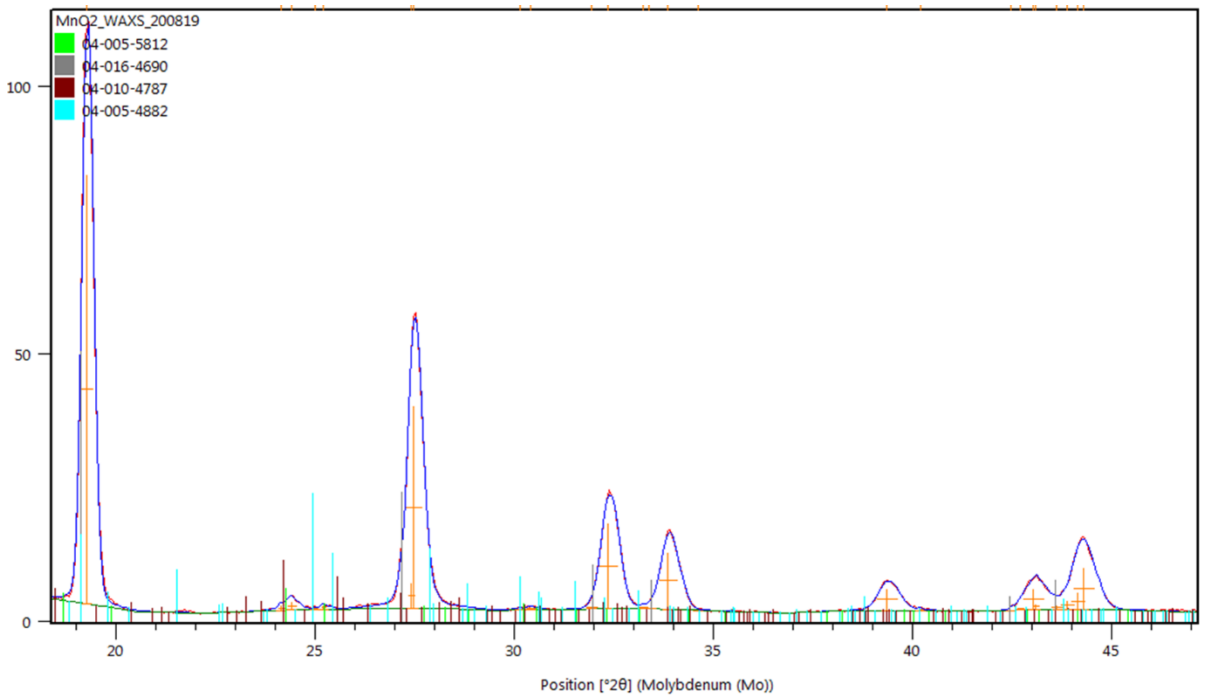

Fig. S18. WAXS analysis on cathode after electrochemical test.

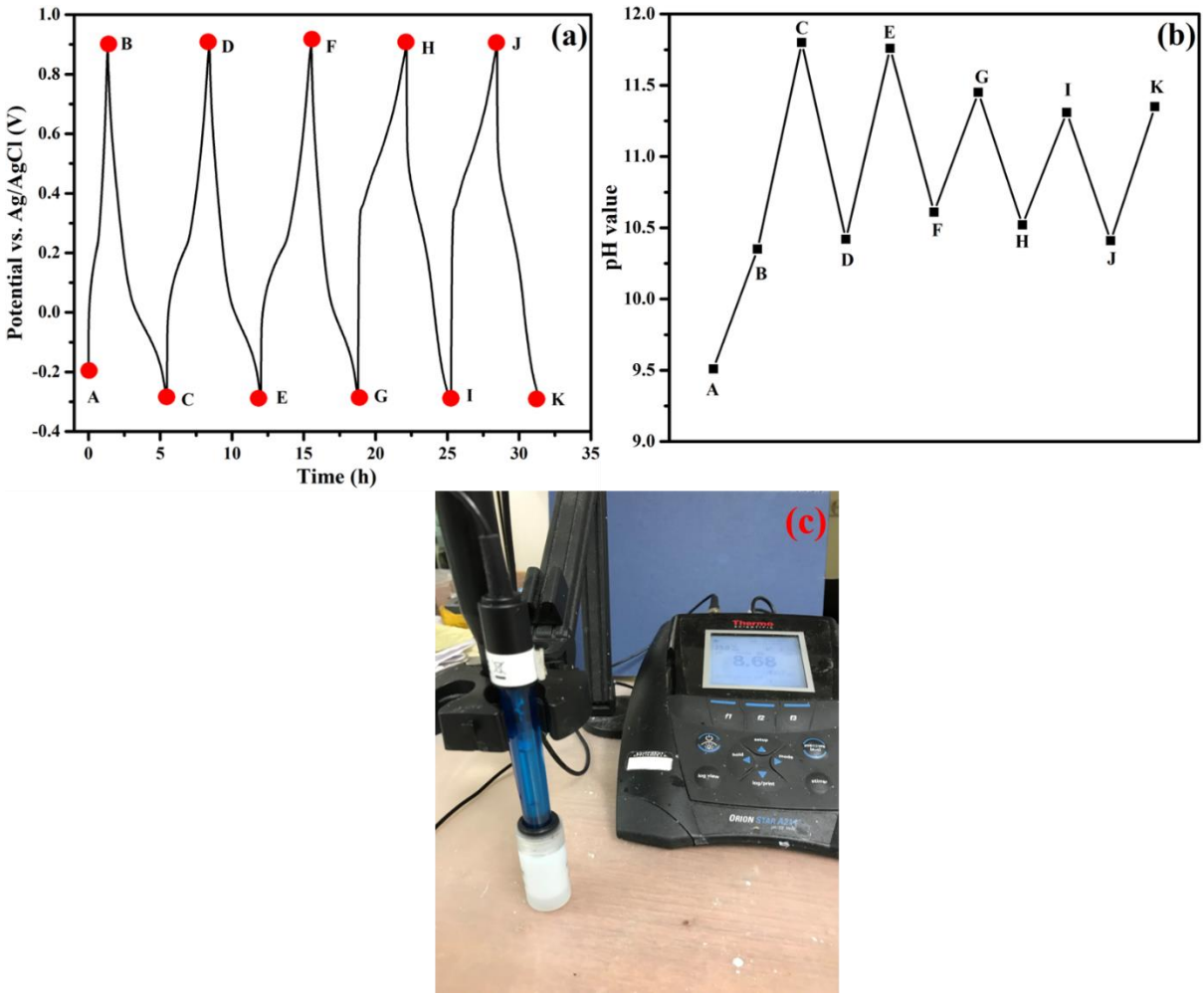

Fig. S19. (a) charge-discharge curves of Zn/MnO_2 battery in three-electrode cell. (b) Corresponding pH value variation of salt-concentrated electrolyte during charge-discharge reaction. (c) Optical image of pH meter.

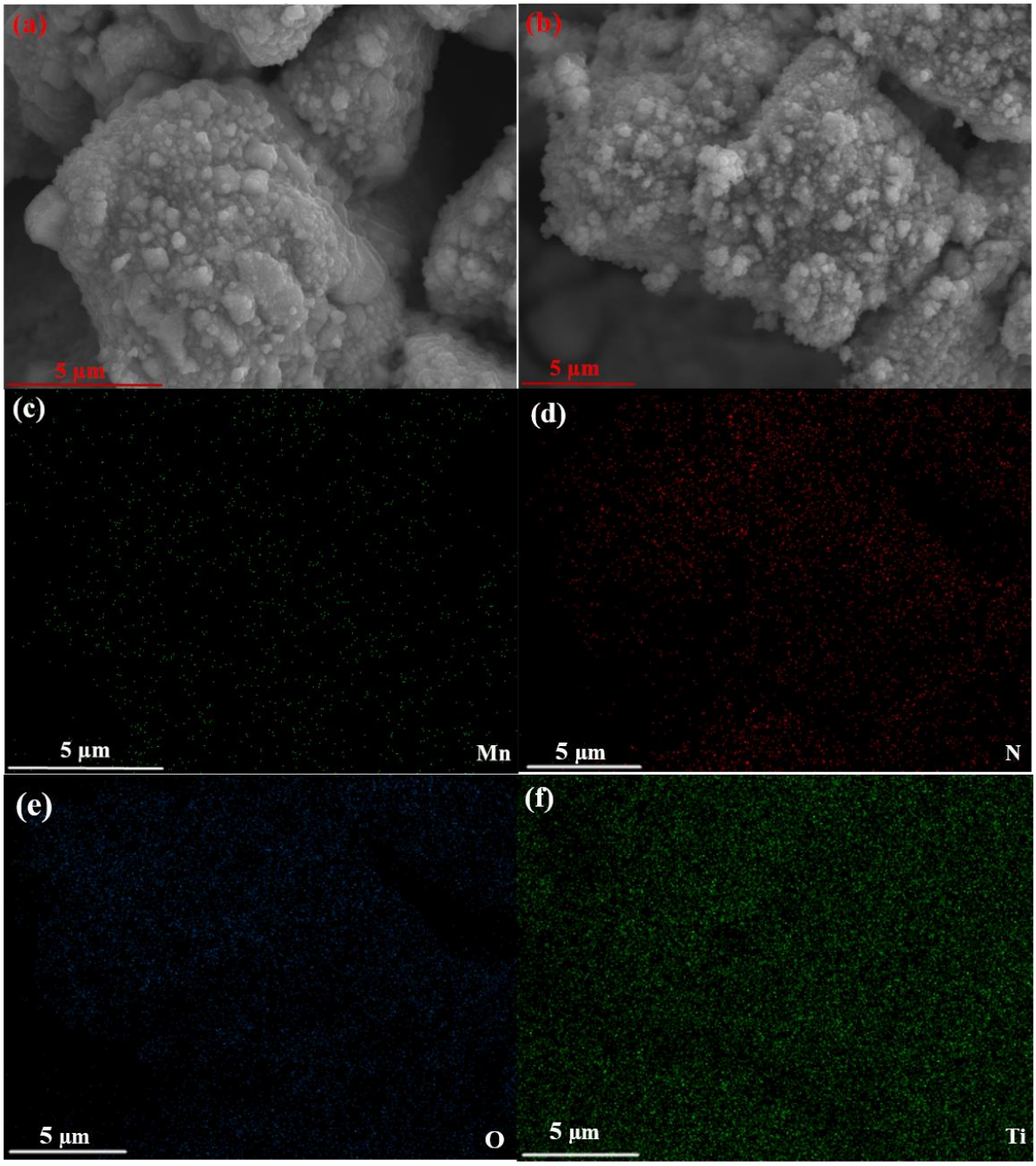

Fig. S20. (a) SEM image of self-supported MnO_2-TiN/TiO_2 cathode after electrochemical test under 5 µm resolution. (b) The other SEM images of self-supported MnO_2-TiN/TiO_2 cathode after electrochemical test under 5 µm resolution and according EDX mappings of (c) Mn, (d) N and (e) O and (f) Ti elements.